

Article

LES Simulation of a Model Gas-Turbine Lean Combustor: Impact of Coherent Flow Structures on the Temperature Field and Concentration of CO and NO

Leonid M. Chikishev ^{1,2}, Dmitriy K. Sharaborin ^{1,2}, Aleksei S. Lobasov ^{1,2}, Artem A. Dekterev ¹ , Roman V. Tolstoguzov ^{1,2}, Vladimir M. Dulin ^{1,2,*}  and Dmitriy M. Markovich ^{1,2}

¹ Kutateladze Institute of Thermophysics, 1 Lavrentyev Avenue, 630090 Novosibirsk, Russia; chlm@itp.nsc.ru (L.M.C.); sharaborin.d@gmail.com (D.K.S.); alexey.lobasov@gmail.com (A.S.L.); dek_art@mail.ru (A.A.D.); enot.roman@gmail.com (R.V.T.); dmark@itp.nsc.ru (D.M.M.)

² Department of Physics, Novosibirsk State University, 1 Pirogov Street, 630090 Novosibirsk, Russia

* Correspondence: vmd@itp.nsc.ru

Abstract: The present paper reports on the numerical simulation of flow dynamics in a model gas-turbine combustor by large eddy simulation in order to evaluate the effect of coherent flow structures on the local fluctuations of gas temperature and local concentrations of NO and CO. The simulations were performed for a generic swirler, based on the design by Turbomeca, for a Reynolds number of 15,000 at normal and elevated inlet temperature and pressure (up to 500 K and 3.4 atm). The simulation data were validated based on the velocity measurements by stereoscopic particle image velocimetry. In order to reveal coherent flow structures, the velocity snapshots were processed by the proper orthogonal method. The temporal coefficients of the decomposition were used to evaluate the conditional sampled spatial distributions of the temperature and species concentration. It is shown that the coherent fluctuations of temperature can locally reach up to 200 K with the fluctuations of NO up to 20%. Thus, the results demonstrate that coherent flow structures in a lean swirl combustor can sufficiently contribute to NO_x emission.

Keywords: gas-turbine combustor; lean methane flame; elevated pressure; particle image velocimetry; large eddy simulation; proper orthogonal decomposition; NO_x emission



Citation: Chikishev, L.M.; Sharaborin, D.K.; Lobasov, A.S.; Dekterev, A.A.; Tolstoguzov, R.V.; Dulin, V.M.; Markovich, D.M. LES Simulation of a Model Gas-Turbine Lean Combustor: Impact of Coherent Flow Structures on the Temperature Field and Concentration of CO and NO. *Energies* **2022**, *15*, 4362. <https://doi.org/10.3390/en15124362>

Academic Editor: Venera Giurcan

Received: 9 April 2022

Accepted: 7 June 2022

Published: 15 June 2022

Publisher's Note: MDPI stays neutral with regard to jurisdictional claims in published maps and institutional affiliations.



Copyright: © 2022 by the authors. Licensee MDPI, Basel, Switzerland. This article is an open access article distributed under the terms and conditions of the Creative Commons Attribution (CC BY) license (<https://creativecommons.org/licenses/by/4.0/>).

1. Introduction

Fuel/air mixing and combustion plays a key role in emission formation of modern combustion chambers of gas turbines. Stabilization of the flame in gas-turbine combustion chambers is provided mainly by swirl and using a pilot flame with separate fuel supply. Many studies have focused on the configuration of the swirler, e.g., the effect of flare section on the Lean Direct Injection (LDI) twin swirlers [1], double-high swirl GTMC configurations with different air mass-flow separation ratios [2], and burner exit geometry (straight or diverging section) [3]. Thereby, the configuration of the swirler can affect the flow field downstream and thus the flame shape and stability. One of the model geometries for gas-turbine combustors is provided by Turbomeca [4]. There are many papers on the flow structure and numerical simulation at normal conditions [5,6]. Albrecht et al. [7] and Liu et al. [8] studied the effects of pilot injection on combustion stability and proved that pilot injection suppresses combustion instability and thereby improves the lean blowoff performance. There are only a few papers on the measurements at elevated pressure and preheating of the air, for example, a DLR dual swirl burner [9,10].

Proper orthogonal decomposition (POD) is used in unsteady combustion studies. For example, a lean-premixed gas turbine with swirl injector was studied numerically [11]. A heat-release structure was examined. It was shown that for the lean methane flame that the first four POD modes correspond to about a half of the heat-release intensity. A model

annular gas-turbine combustor for methane–air and ethylene–air blends was studied by Zetterval et al. [12] It was shown that the heat-release for different burners is affected by a large-scale azimuthal mode. Semlitsch et al. [13] have studied entropy and vorticity generation in a realistic gas turbine combustor. They have revealed that 10–20 POD modes are enough to represent low-frequency pulsations, whereas high-frequency fluctuations in the near wall region remains under-resolved.

Agostineli et al. recently studied the impact of wall heat transfer in LES on the flame dynamics in a swirled combustion chamber [14]. The fuel mass flowrate was 0.2 g/s, whereas the air mass flowrate was 4.29 g/s, providing a global equivalence ratio of 0.8 for the PRECCINSTA design [5,15]. It was demonstrated that LES is a robust approach to study complex swirling flows with combustion in gas-turbine-related geometries [16–18] or to evaluate complicated flame/flow interaction for prediction of thermoacoustic instabilities [19,20].

Previously, it was shown that absence of the central jet leads to large destabilization of the flow [21,22]. The swirl cone becomes more unstable itself without a central jet. Previously, Dunham et al. [23] presented a comparison of the LES and URANS CFD approaches applied to this flow. Both methods show reliable features of the mean flow, but only LES captured the change in flow stability that had been found for the with-jet and no-jet configurations.

The major objective of this paper is to understand the effect of large-scale coherent flow structures on the temperature field fluctuations and local concentration of pollutants (mainly NO_x and CO) in a model swirl-stabilized lean combustor, based on the design by Turbomeca, by means of LES. The structure of the flow field has been experimentally studied previously by stereoscopic particle image velocimetry (stereo PIV) with the simultaneous visualization of the flame front shape by OH planar laser-induced fluorescence (OH PLIF). The obtained experimental data are used for the validation of LES, whereas the numerical data allow to visualize the impact of coherent flow structures on the concentration of NO and NO₂ in the flow.

2. Experimental and Numerical Approach

2.1. Combustor

The model combustion chamber with optical access is described in detail in [21]. The burner provides the main premixed combustion zone and a pilot central flame. The nozzle geometry is similar to that of Midgley et al. [22] for the case of a radial entry slot angle of 30°. The swirler's nozzle diameter was 37 mm. The swirler has two fuel channels: a pilot channel representing the central fuel jet (inner diameter of 5.8 mm) and the main fuel channel representing the holes between the vanes of the swirler. The pilot channel contraction reproduces the design of Midgley [23]. Methane was used as the fuel. The global equivalence ratio of the flames was 0.33. The flowrates ratio between the pilot and main fuel was 0.3, which is close to the lean blowoff conditions. The chamber outlet is organized by an axisymmetric contraction choked nozzle with water cooling. The optical windows are protected via a film cooling by air inside the combustion chamber to prevent overheating and particle contamination during long-term operation.

The flowrates were controlled using Bronkhorst High-Tech mass flow meters. The Reynolds number for cold non-reacting flow was 1.5×10^4 based on the bulk velocity of the main air and its viscosity. A cylindrical plenum chamber was used for the flow settle before the combustion chamber using a perforated plate and collecting the combustion air flow from four radial pipe lines. To prevent an unsteady air supply to the radial swirler, the length of the plenum chamber was 120 mm. The plenum chamber was equipped with an electric wire heater to preheat the main air flow. The TiO₂ particles were introduced to the main air flow upstream of the plenum chamber to carry out the PIV measurements. The combustion regimes under consideration are summarized in Table 1.

Table 1. Flame parameters.

Air Flowrate (g/s)	Fuel Flowrate Main (g/s)	Fuel Flowrate Central (g/s)	Equivalence Ratio	Inlet Air Temperature (K)	Pressure (atm.)
8	0.12	0.036	0.33	293	1
8	0.12	0.036	0.33	500	2
8	0.12	0.036	0.33	500	3.4

2.2. Stereo PIV and PLIF Equipment

Stereoscopic PIV system was used to provide flow measurements. We used a double-head pulsed Nd:YAG laser from Beamtech (Vlite 200) with 6 ns pulses of 200 mJ energy per each pulse at 532 nm wavelength and two ImperX cameras (Bobcat IGV-B2020) with 4 Mpix resolution and dynamic range of 8 bits. The camera's lenses were equipped with bandpass optical filters centered at 532 nm with full width at half maximum of 10 nm. To provide OH PLIF measurements, the LaVision Tunable LIF Flame master system consisted of tunable dye laser (Sirah Precision Scan) with pump laser (Nd:YAG QuantaRay system) and sCMOS camera with IRO intensifier equipped with a UV lens and band-pass optical filter (300–320 nm) was used. The laser system was tuned to the wavelength of 283 nm to excite the OH fluorescence for the $Q_1(8)$ line of the $A^2\Sigma^+ - X^2\Pi(1-0)$ band. Two laser sheets crossed the flow at the central jet axis. To synchronize the PIV/PLIF systems, an external TTL generator was used. For the spatial calibration of the cameras we used a calibration target. It was done prior to and after the experiments. Non-uniform UV-laser sheet energy distribution and shot-to-shot intensity variations were taken into account during PLIF data processing using a CCD camera (ImperX Bobcat IGV-B4820), which monitored a part of the intensity reflected to the calibration cuvette with a Rhodamine solution.

2.3. Numerical Simulation Approach

The wall adapting local eddy-viscosity model was exploited for the turbulent flow simulation. The partially premixed combustion was modelled by a non-adiabatic flamelet generated manifold (FGM) model. The ideal-gas equation of state was used. The FGM tables were generated using GRI-MECH 3.0 [24], a detailed reaction mechanism that contained 53 species and 325 reactions. The radiative heat transfer was simulated employing the DO (discrete-ordinates) grey radiation model [25,26]. The absorption coefficient, which is a function of local gas composition and temperature, was calculated using the weighted sum of grey gases model (WSGGM) with a domain-based length scale. Weighting factors of the model are valid for a temperature range $600 \leq T \leq 2400$ K [27].

The simulations were carried out using unstructured computational grids with about 12 million nodes (see Appendix A). The LES computational domain is shown in Figure 1. Several layers of prismatic elements were created at the burner walls for better resolution of the boundary layer. The discretization of the transport equations was performed based on a finite volume method. Pressure–velocity coupling for incompressible flow was achieved by the SIMPLEC procedure [28]. For each variable, the spatial discretization scheme was of the second or higher order. The central differencing scheme was adopted for the momentum to obtain a significantly lower dissipation than a second-order upwind scheme. A bounded second-order accurate backward Euler scheme was selected for time integration.

All cases were initialized using the results of a RANS steady-state calculation with SST k-omega turbulence model. The computational time needed to obtain statistically steady flow was significantly reduced by this approach. The time step used for unsteady calculations was 5×10^{-5} s. After achieving the quasi-steady operational regime (about 0.25 s simulated time), the additional 10,000–15,000 time-steps were run to collect the statistical data for all variables of interest. The final sampled time was between 0.5 and 0.75 s for different cases. The HPC Cluster, including 64 and 128 cores, depending on the considered case, was used for calculations.

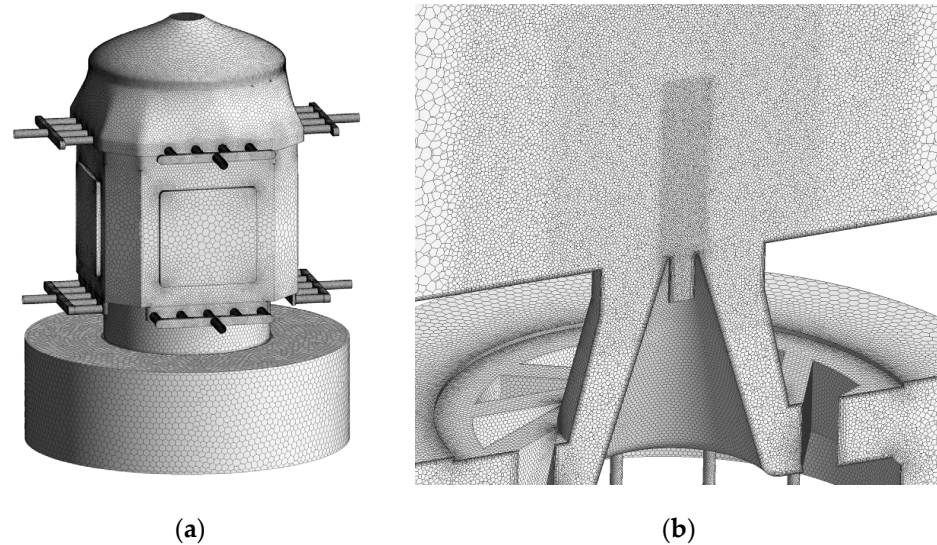


Figure 1. Computational mesh on the domain surface (a) and mesh in the section of the burner (b).

2.4. Data Processing

To obtain and evaluate the PIV data, “Actual Flow” software was used. PIV data were processed using an iterative cross correlation algorithm with continuous shift and deformation of the interrogation areas [29] (final integration area size 32×32 pixels; spatial overlap 50%). The three component velocity fields were reconstructed using two mapping functions and corresponding 2D velocity fields [30]. The calibration target was used to build mapping functions for each PIV camera.

The snapshot POD (proper orthogonal decomposition) approach was used to process the instantaneous velocity data ensembles [31], obtained with singular value decomposition (SVD) applied to the data matrix [32]. The conditional sampled velocity distributions were obtained using the first two POD modes, since the coherent pulsations are dominated in the flow dynamics. The zero correlation between the stochastic and coherent pulsations was achieved due to SVD providing spatial and temporal orthonormality. Afterwards, the concentration and temperature fields were also conditionally sampled to obtain the coherent pulsations [33,34].

3. Results

3.1. Flow Structure

Figure 2 shows the mean velocity fields for the different cases according to Table 1. PIV data and LES results are presented. The out-of-plane velocity component is visualized by color. The velocity data were normalized by the bulk velocity U_0 of the main air flow. The bulk velocity was $U_0 = 6.436$ for 1 atm and 293 K, $U_0 = 5.43$ for 2 atm, and $U_0 = 3.2$ for 3.4 atm. The y -axis corresponds to the axis of the pilot nozzle with the origin at $(0, 0)$, defined at the center of the pilot nozzle outlet. In general, there is a good agreement between the time-averaged velocity data obtained from the PIV experiment and by LES. There is an annular swirling jet, which comes from the swirler’s nozzle exit and surrounds a central recirculation zone (CRZ). The width of the recirculation zone reaches its maxima at a distance of approximately $0.6D$ for all considered cases.

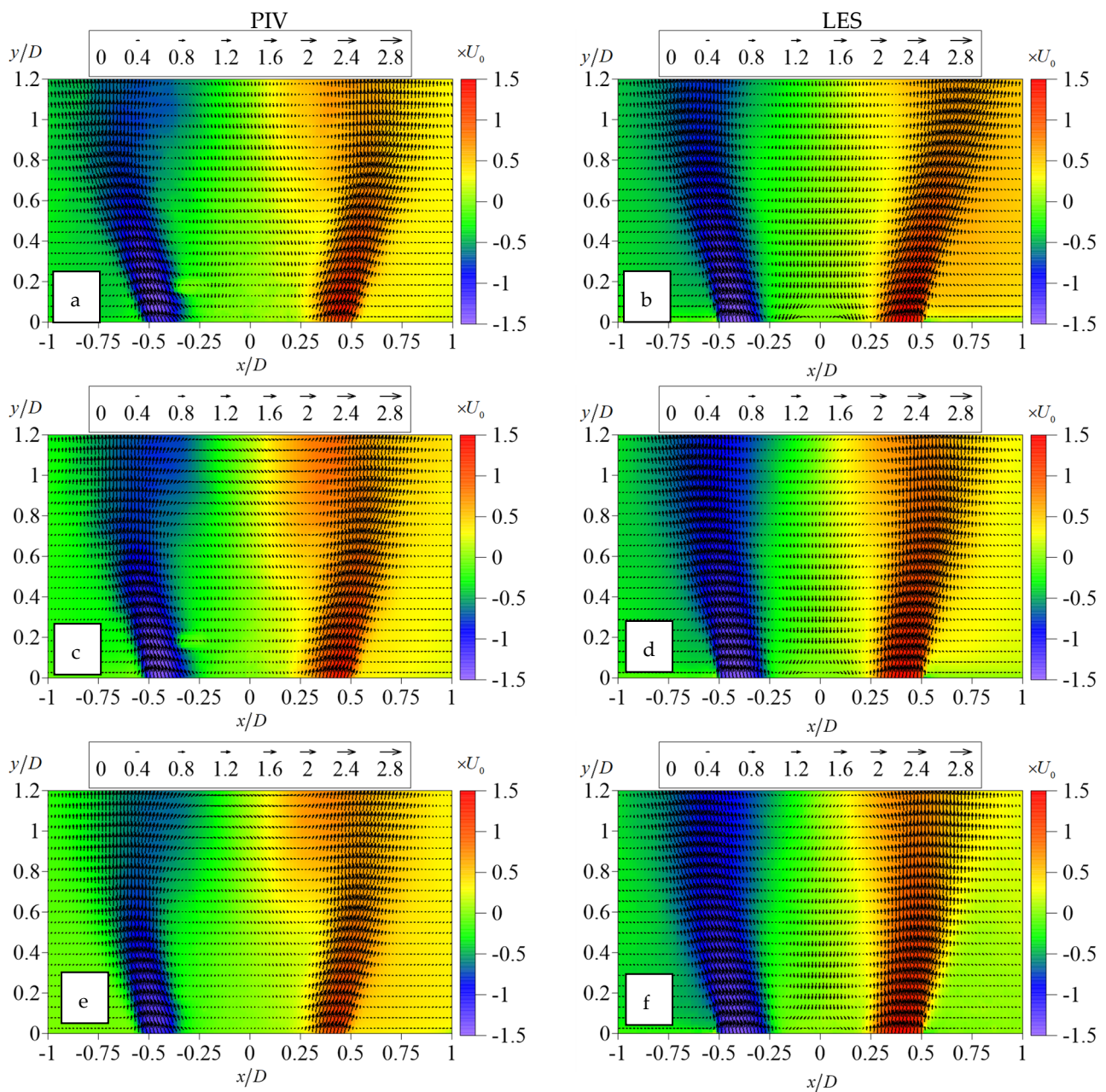


Figure 2. Experimental data and numerical simulation of the mean flow field for methane–air flames at different pressure conditions: (a,b)—1 atm, 293 K; (c,d)—2 atm, 500 K; (e,f)—3.4 atm, 500 K.

Figure 3 compares the plots of the different velocity components for three cross-sections at different distances from the nozzle exit (namely, 0.2D, 0.5D, and 1D). There is a reasonable agreement between the experimental and numerical data for the main annular flow. There is no trace of the central pilot jet for the PIV data because the fuel flow was not seeded by the TiO_2 tracers. Besides, the correspondence between the transversal velocity component for the cross-section at 1D is bad, because its magnitude is about 10% of the bulk velocity, which is of the order of the PIV accuracy.

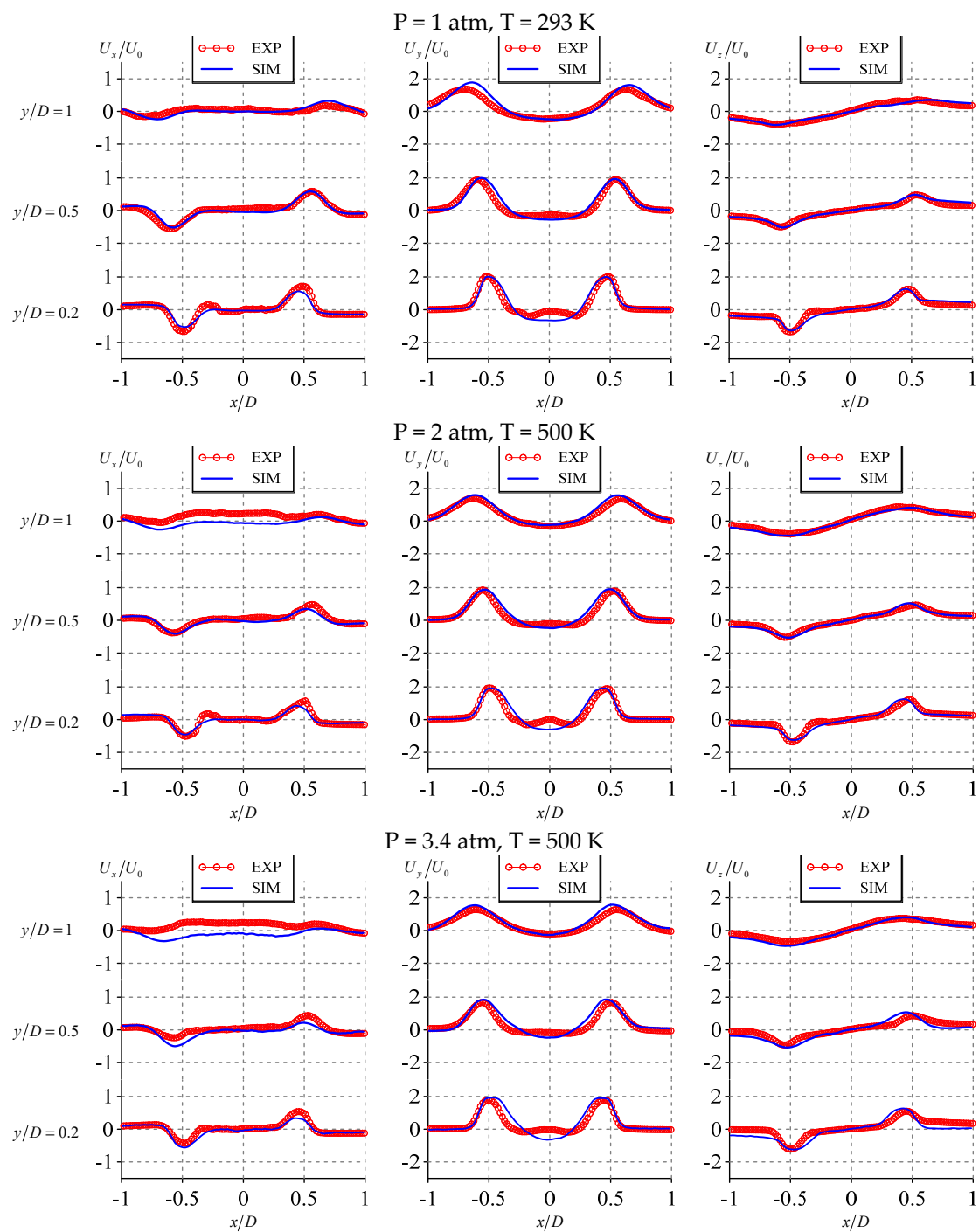


Figure 3. Comparison of the mean velocity profiles measured by PIV and modelled by LES: radial component in the left column, axial component in the middle column, and azimuthal component in the right column.

Figure 4 plots the normalized spatial distributions of the standard deviation of the axial velocity fluctuations. Despite the PIV data being considerably noisier, it is seen that for each flow case there are two regions of intensive velocity fluctuations in the inner and outer shear layers of the main annular flow. Both the experimental and numerical data demonstrate the trend in the fluctuations' magnitude decrease with pressure. The standard deviation locally exceeds $0.6U_0^2$ for the atmospheric pressure, whereas for the case of 3.4 atm it is below $0.3U_0^2$. Figure 5 provides the examples of the instantaneous

velocity snapshots with the OH PLIF images and temperature fields for the experimental and numerical data, correspondingly, to demonstrate the flame front location.

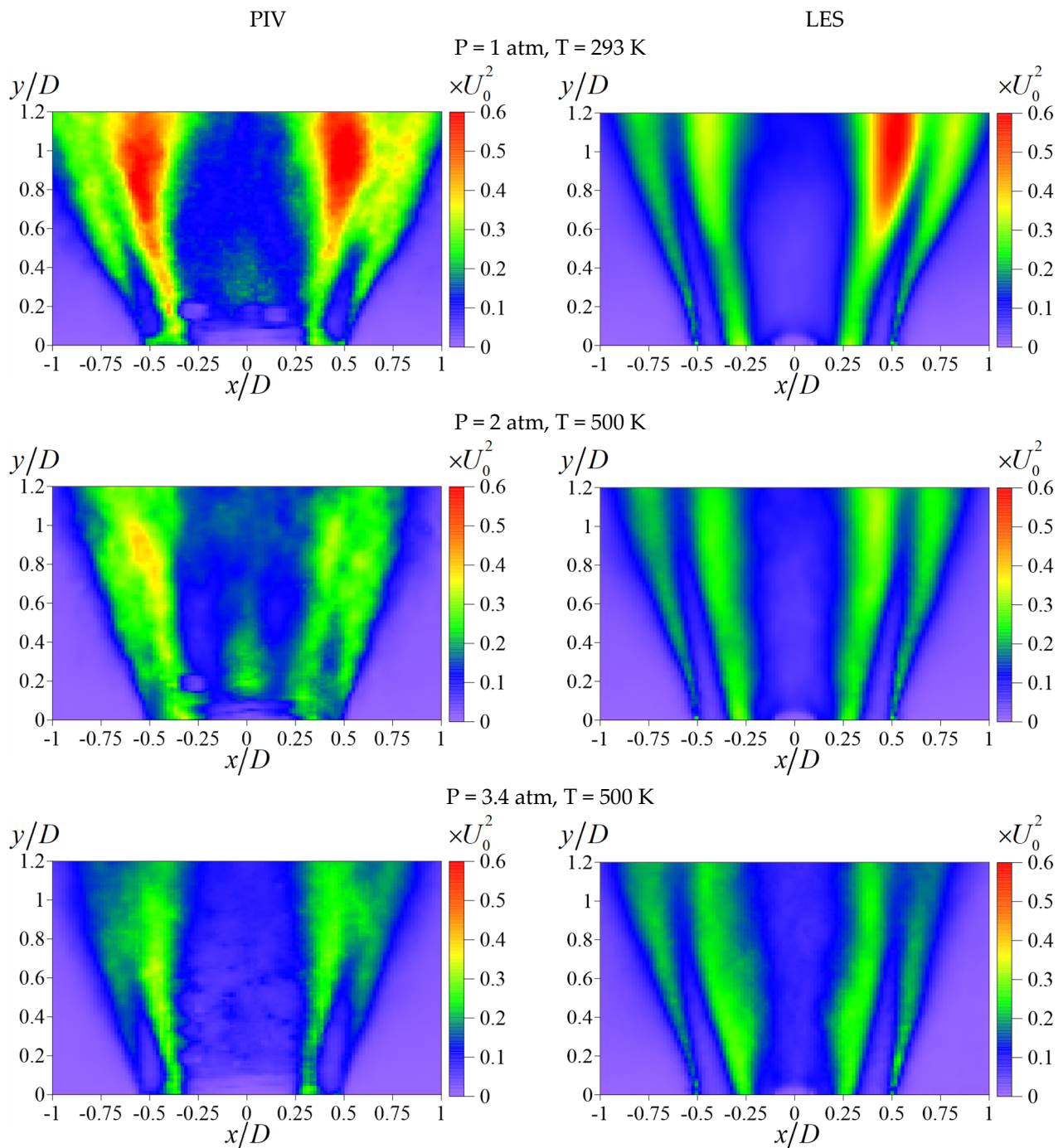


Figure 4. Standard deviation of the axial velocity fluctuations for PIV and LES.

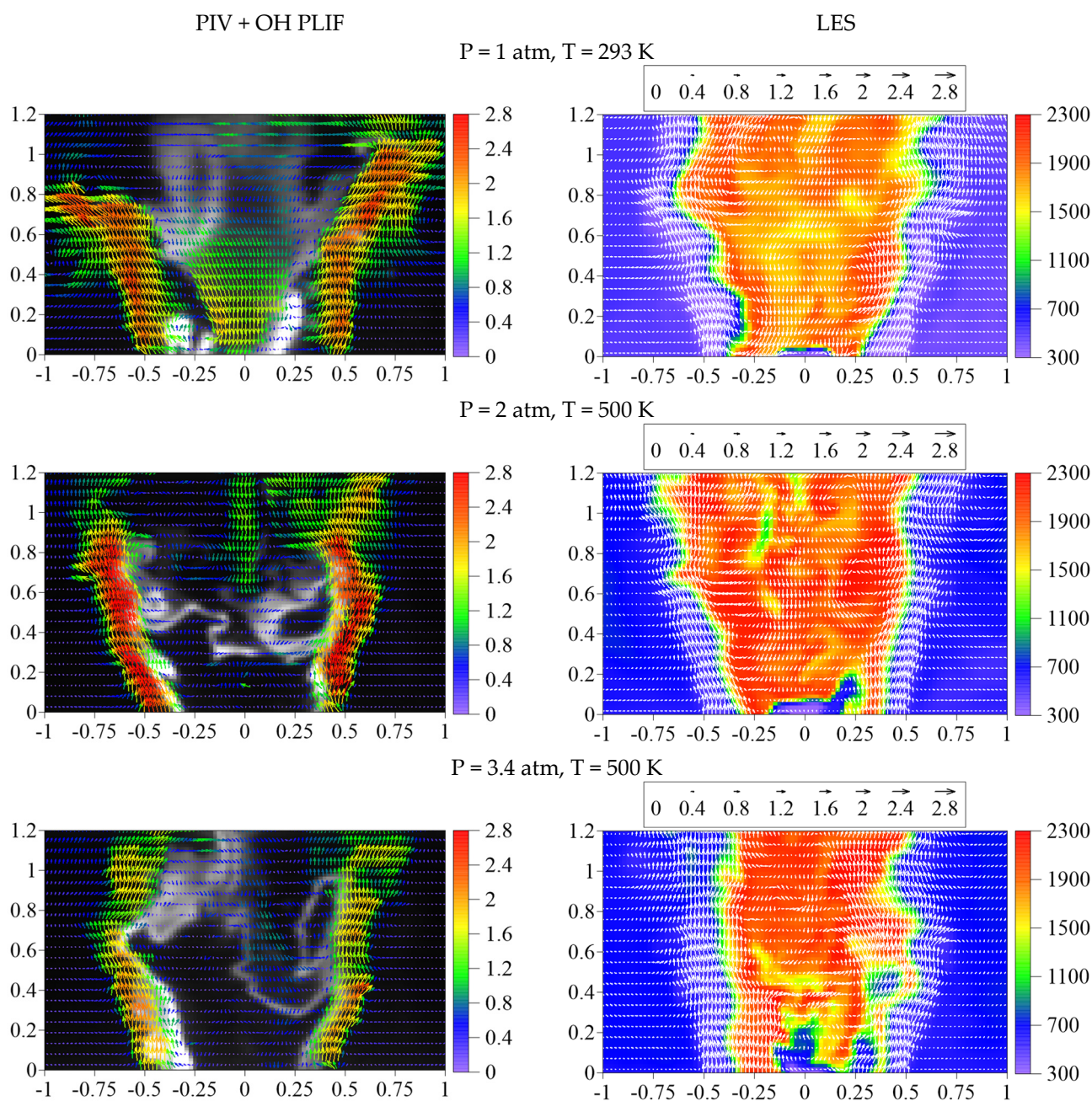


Figure 5. Instantaneous velocity field and OH arbitrary concentration (**left** column) and simulated instantaneous and temperature field (**right** column) depending on pressure and preheat temperature.

By analyzing the instantaneous velocity fields and OH signal distribution in Figure 5, one can see that the central pilot jet plays an important role in flame stabilization. The flame front penetrates inside the swirler's nozzle and also surrounds the region between the central jet and the CRZ. The numerical simulation shows that the central jet breaks up immediately after the exit from the central nozzle. With the growth of inlet in the combustion chamber the flame front above the central jet is slightly shifted downstream and inside the swirler it is closer to the nozzle wall (i.e., the flame is wider). Instantaneous temperature fields simulated by the LES approach demonstrate that hot gases are concentrated in the CRZ. With the increase in pressure, the central jet penetrates further inside the CRZ, which is in agreement with the experimental results. The instantaneous snapshots also demonstrate that there are large-scale vortex structures present both in the inner and

outer shear layer, which deform the flame front and should be important for local heat and mass transfer.

3.2. Temperature and Carbon and Nitrogen Oxides Concentration

The present sub-section discusses the time-averaged values and root-mean-square deviation of the fluctuations of the temperature and carbon and nitrogen oxides, obtained from LES. The temperature data are shown in Figure 6. The hot gases are concentrated in CRZ, with the highest magnitude of the temperature fluctuations (up to 30 % of maximum mean temperature values) along the main annular jet and around the origin of the central pilot jet. The magnitude of the temperature fluctuations does not change strongly with the increase of the pressure inside the chamber. However, it is seen that the region of the temperature fluctuations in the CRZ around the central jet becomes much wider. The elevated inlet temperature of the main air flow results in an overall increase in the time-averaged temperature, including CRZ and the outer recirculation zone between the main annular jet and side walls of the chamber.

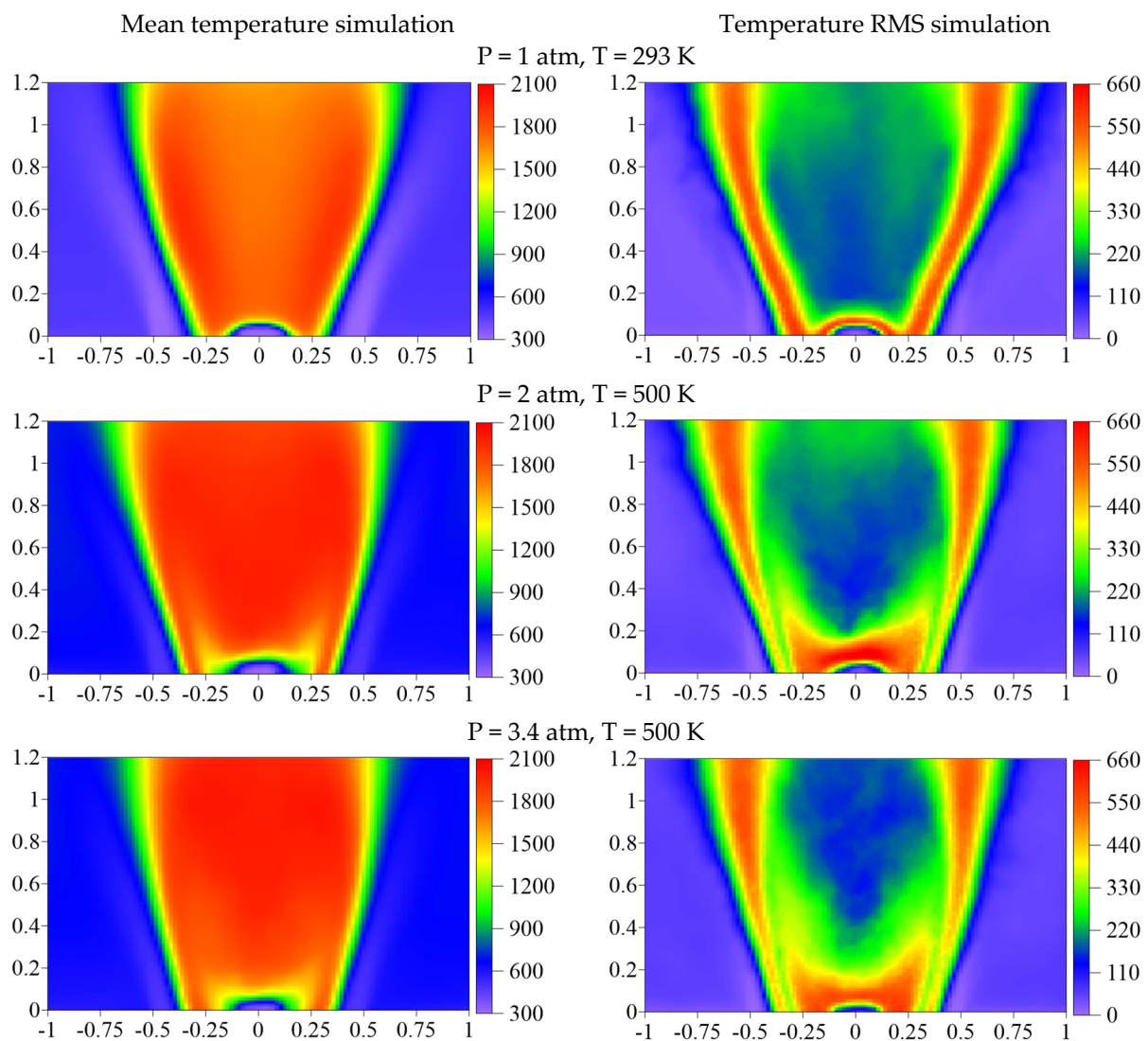


Figure 6. Mean temperature fields and RMS of the temperature fluctuations evaluated by the LES approach.

The effect of the elevated pressure and temperature on carbon monoxide is strong, as demonstrated in Figure 7. There is a dramatic increase in CO concentration with an

increase in pressure and temperature. Whereas, for the normal conditions, the mean CO concentration and RMS of its fluctuations are high in the inner mixing layer, with the increase in pressure and inlet temperature in the regions of the high values shifting towards the CRZ. Therefore, the combustion efficiency close to the swirler is strongly reduced.

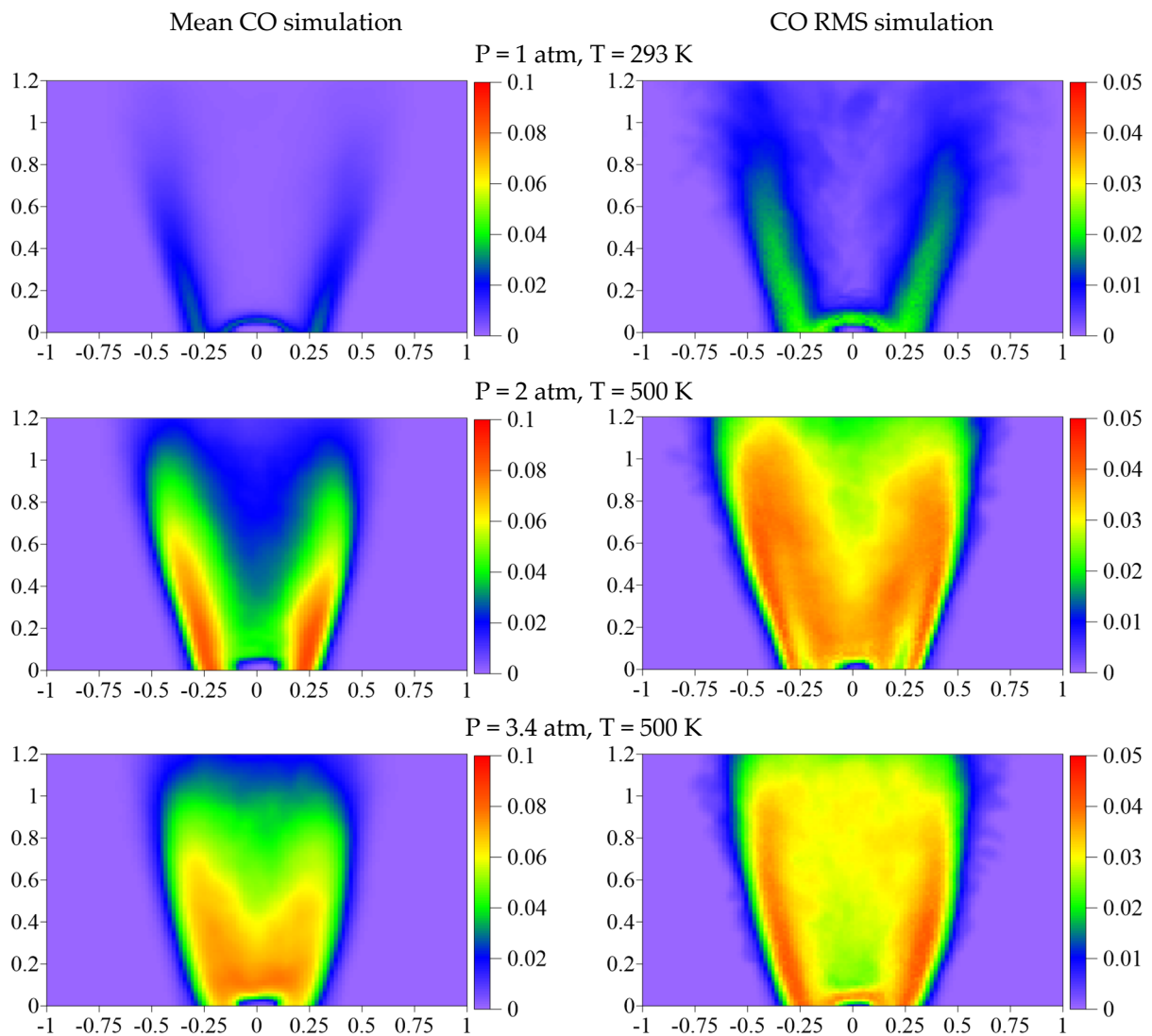


Figure 7. Mean CO concentration fields and RMS of the concentration fluctuations evaluated by the LES approach.

The time-averaged data for the CO_2 concentration and RMS of the concentration fluctuations (see Figure 8) support the conclusion that on average the combustion efficiency near the swirler is reduced for the elevated conditions. For the normal conditions, the mean CO_2 distribution inside the CRZ appears to be more uniform in comparison with the cases of higher temperature and pressure. The increase in pressure from 2 to 3.4 atm further reduces the combustion efficiency around the pilot jet (at the bottom of the RCZ). This observation is supported by the intensity of the CO_2 concentration fluctuations. The region of high RMS value is much broader for the elevated temperature and pressure.

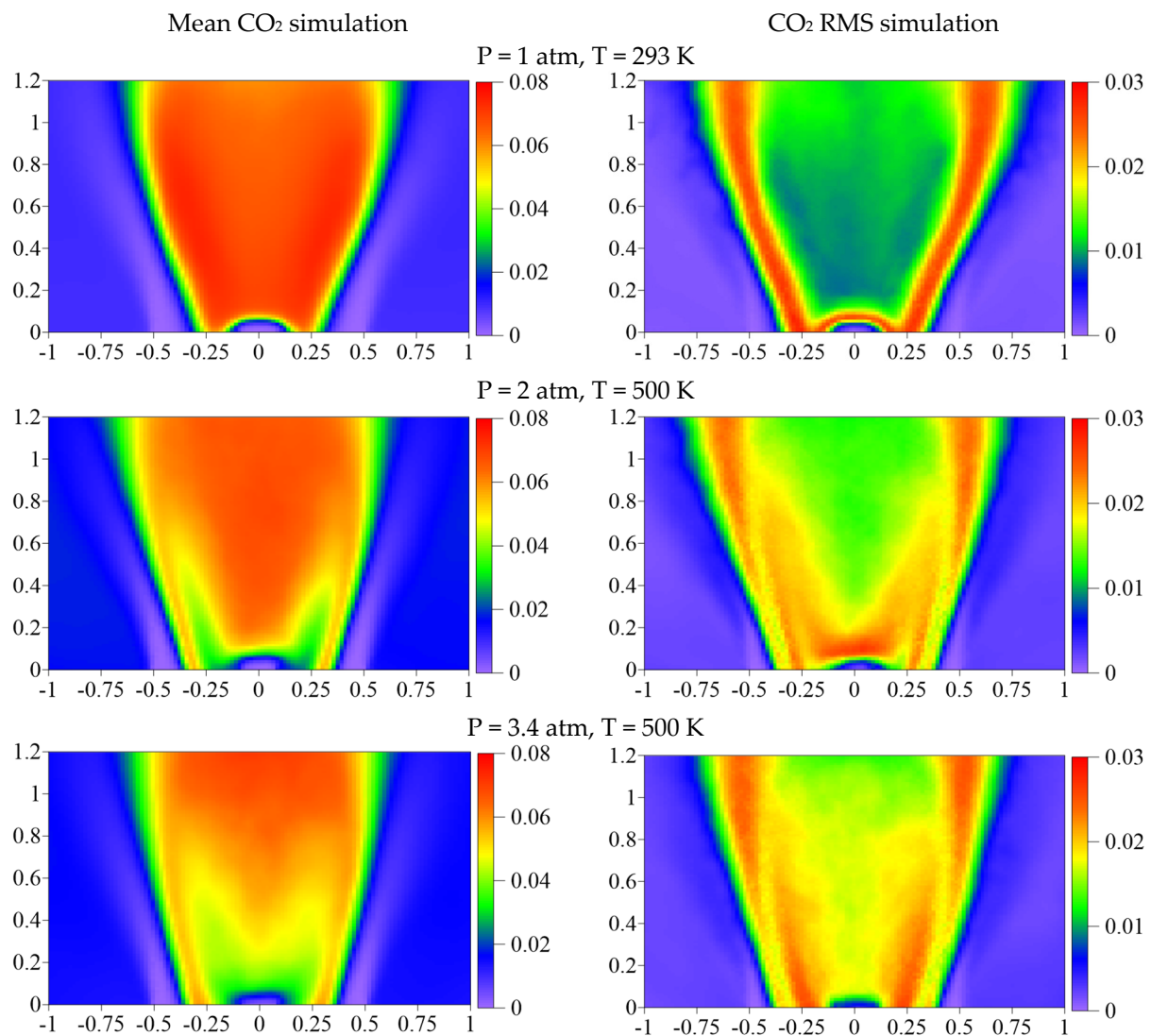


Figure 8. Mean CO₂ concentration fields and RMS of the concentration fluctuations evaluated by the LES approach.

The time-averaged values and RMS of the fluctuations of the NO and NO₂ concentration fields are shown in Figures 9 and 10, respectively. Please note that for some cases the RMS values can locally exceed 50% of the average value. It should be noted that the concentration of NO₂ near the swirler is much smaller than NO. For the flame at normal conditions, the time-averaged NO is present mainly inside the CRZ, where the hot combustion products with the remaining oxygen and nitrogen circulate. Due to the unsteady turbulent flow inside the CRZ, the RMS of the NO concentration locally reaches 35%. For this flow case the mean NO₂ concentration has the highest magnitude along the inner shear layer and appear to grow in the upper part of the CRZ due to NO oxidation downstream. The RMS of the NO₂ concentration fluctuations is also high in the inner shear layer.

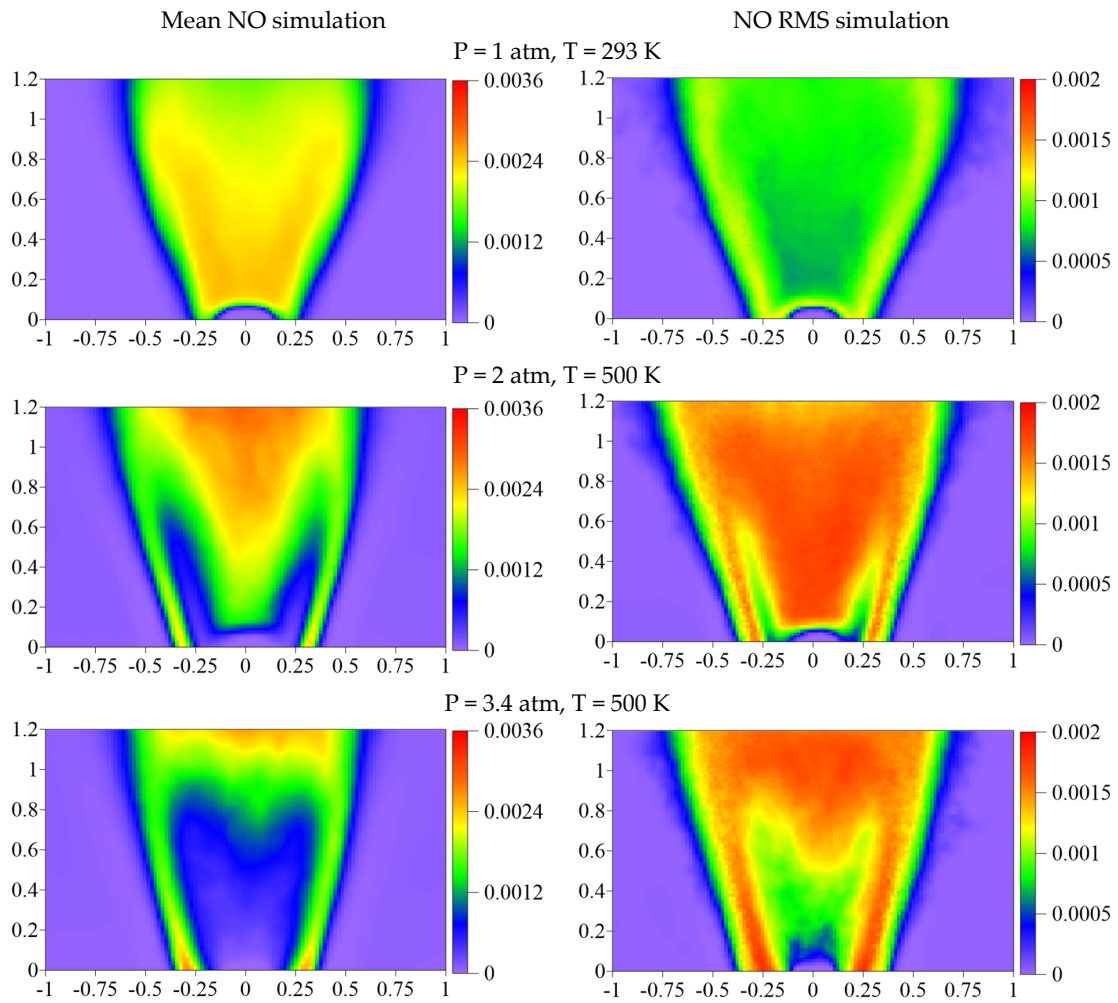


Figure 9. Mean NO concentration fields and RMS of the concentration fluctuations evaluated by the LES approach.

For the elevated temperature and pressure conditions, the maximal values of the mean NO concentration shift downstream. Therefore, in the bottom part of the CRZ around the pilot jet the concentration of NO decreases. The same trend is observed for the RMS of the NO concentration fluctuations. It is also observed that the elevated conditions result in a dramatic increase in the NO₂ concentration and RMS of its fluctuation in the flame at the exit of the swirler’s nozzle. It could be caused by the flame shifting further inside the nozzle for higher pressure and a worse fuel–air mixing upstream of the flame front.

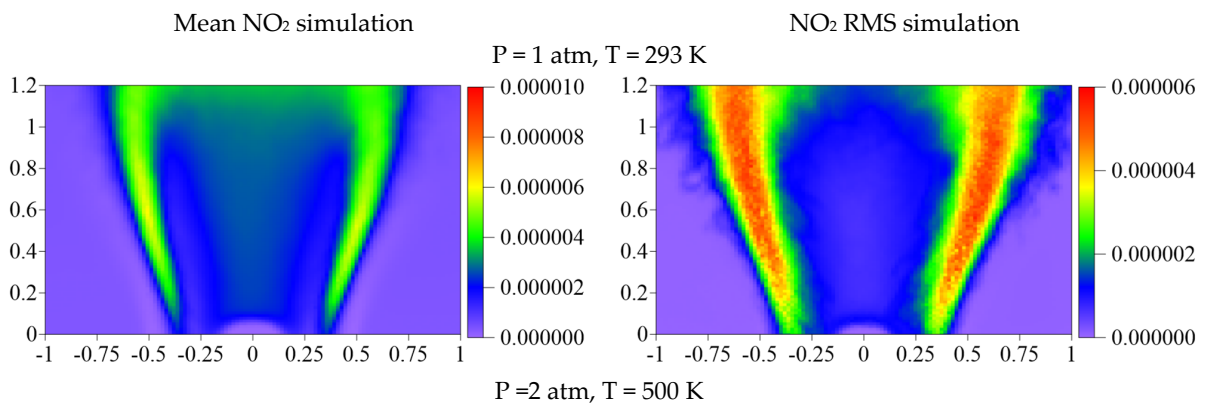


Figure 10. Cont.

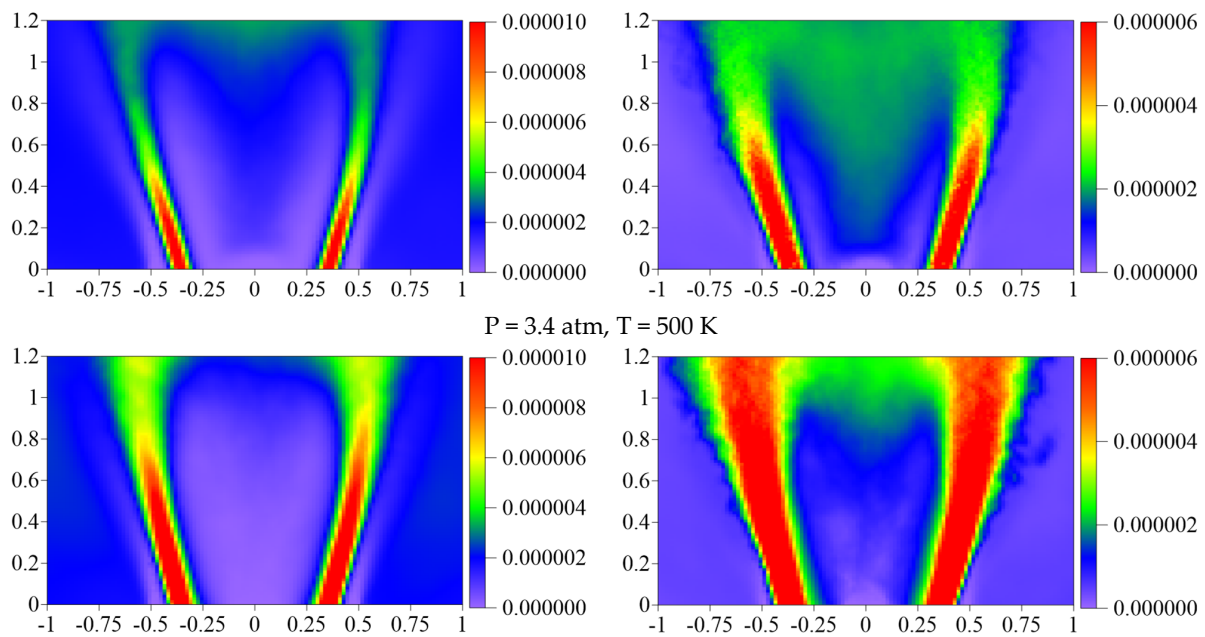


Figure 10. Mean NO_2 concentration fields and RMS of the concentration fluctuations evaluated by the LES approach.

3.3. Coherent Flow Structures and Conditionally Sampled Data in Vertical Cross-Sections

This sub-section reports on the coherent flow structures effect on the local variation of the gas temperature and concentration of the carbon and nitrogen oxides. Therefore, the POD analysis is applied to 1000 snapshots of the LES data downsampled for a frame rate equal to 1 kHz. The obtained POD spectra are presented in Figure 11. It is found that the first few POD modes correspond to two different types of large-scale velocity fluctuations, namely, nearly symmetrical and asymmetrical modes with respect to the swirler axis. Such modes are discussed in detail in our previous experimental study [34,35]. Further, such modes are referred to as a longitudinal and transverse hydrodynamic modes.

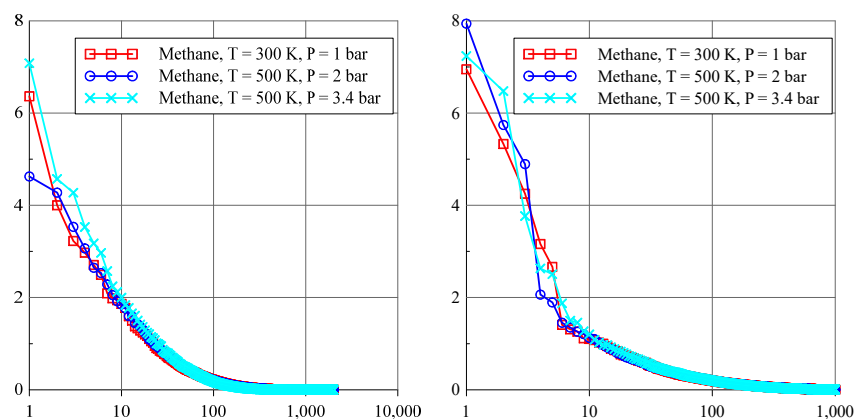


Figure 11. POD spectra of the LES velocity snapshots for vertical (left) and horizontal cross-sections of the flow at 1D (right).

Temperature variations corresponding to the first and second POD mode are presented in Figure 12. For the cases of 1 and 2 atm pressure, the first and second POD modes correspond to the longitudinal and transverse hydrodynamic modes, respectively. For the case of 3.4 atm, both the first and second POD modes are related to the longitudinal hydrodynamic modes. The spatial distributions of the modes are not perfectly symmetric or antisymmetric due to the finite number of the used snapshot and limited duration

of the considered time interval. Nevertheless, they are sufficient to analyze the impact of different hydrodynamic modes on the local variation in temperature and carbon and nitrogen oxides concentration.

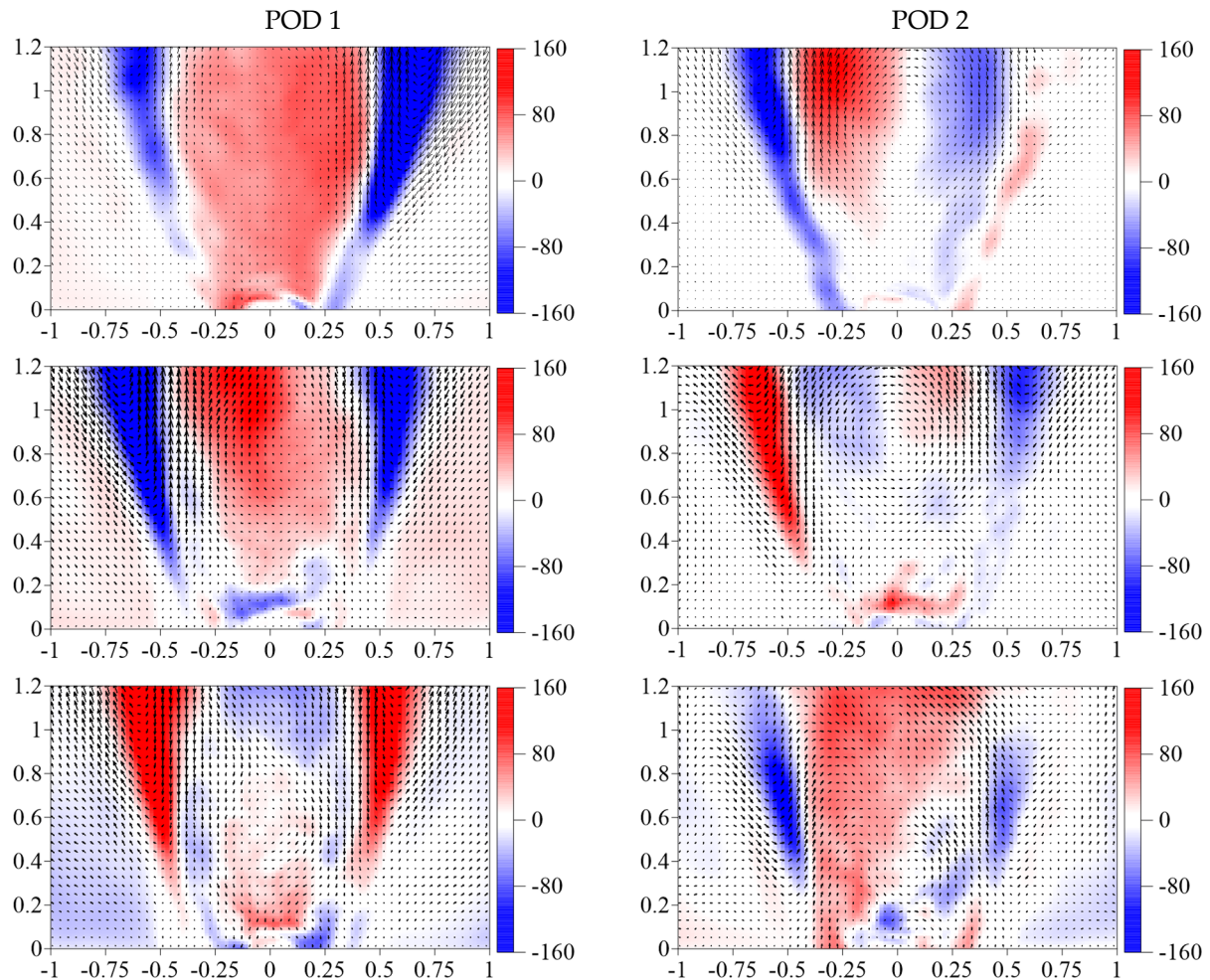


Figure 12. The first and the second POD modes with the conditional sampled temperature: the first line—1 atm, 293 K; the second line—2 atm, 500 K; the third line—3.4 atm, 500 K.

The conditional sampled values of the temperature fluctuations are shown in Figure 12. According to the first POD mode (longitudinal hydrodynamic mode for all considered cases) the highest coherent temperature fluctuations are induced in the inner shear layer and inside the recirculation zone. In the shear layer the amplitude is above 150 K. The transverse hydrodynamic mode (second POD mode for the cases of 1 atm and 2 atm) is also related with similar magnitude of the temperature variation in these regions. According to the conditional sampled data, the elevated conditions results in a strong increase in the coherent fluctuations of the CO concentration (Figure 13). The spatial distributions of the conditionally sampled CO₂ concentration (Figure 14) fluctuations are similar to those of the temperature fluctuations and appear to be due to the non-uniform heat release.

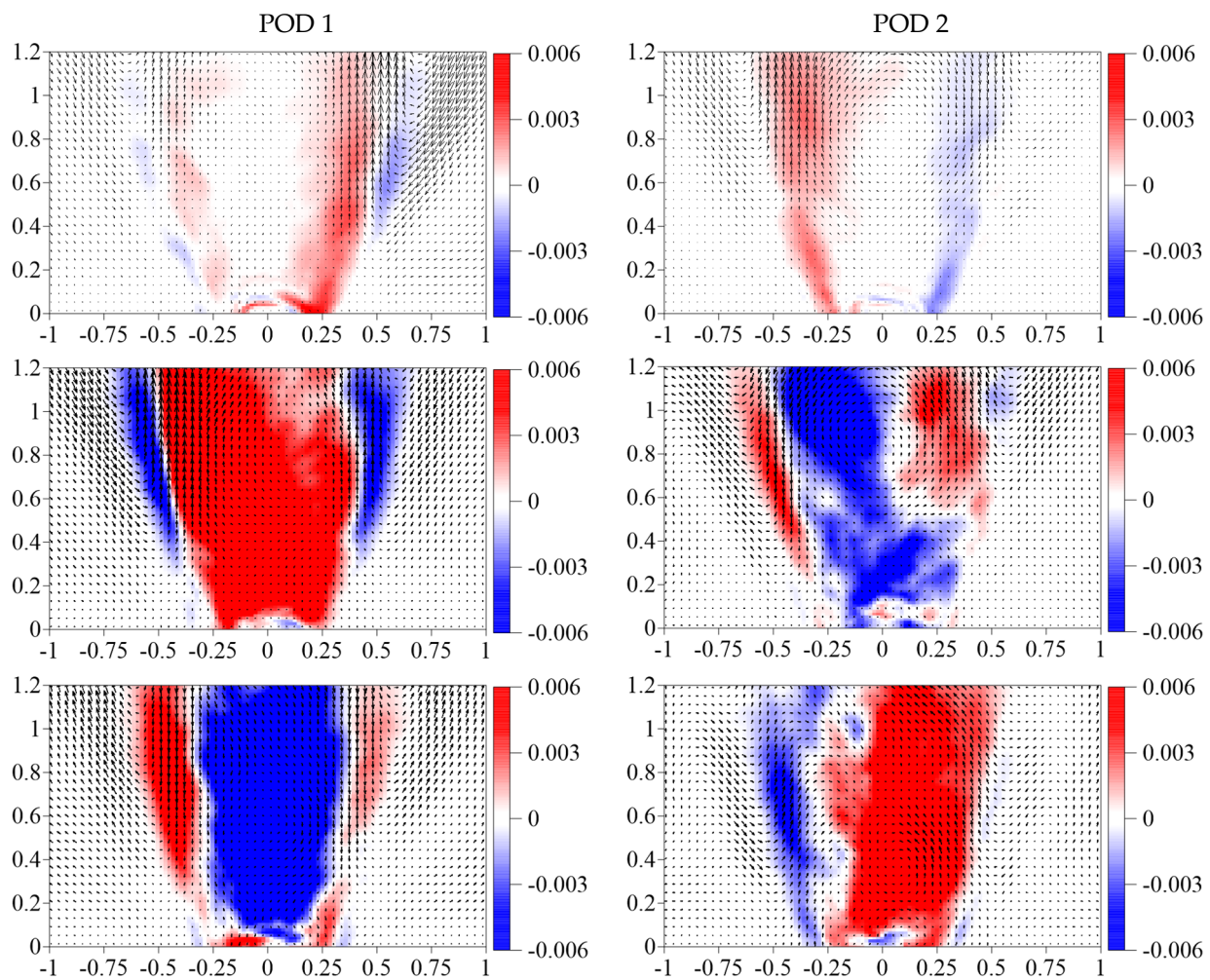


Figure 13. The first and the second POD modes with the conditionally sampled CO concentration: the first line—1 atm, 293 K; the second line—2 atm, 500 K; the third line—3.4 atm, 500 K.

The distributions of the conditionally sampled NO to NO₂ concentration fluctuations are shown in Figures 15 and 16, respectively. According to the NO data for the atmospheric conditions, the longitudinal hydrodynamic mode can be responsible for the coherent fluctuations of the nitrogen monoxide concentration with an amplitude above 400 ppm (with the maximal time-averaged concentration of 2000 ppm). The amplitude of the fluctuations is even greater for the elevated pressure and temperature. According to the spatial distributions, the intensive fluctuations are related to the unsteady combustion in the CRZ.

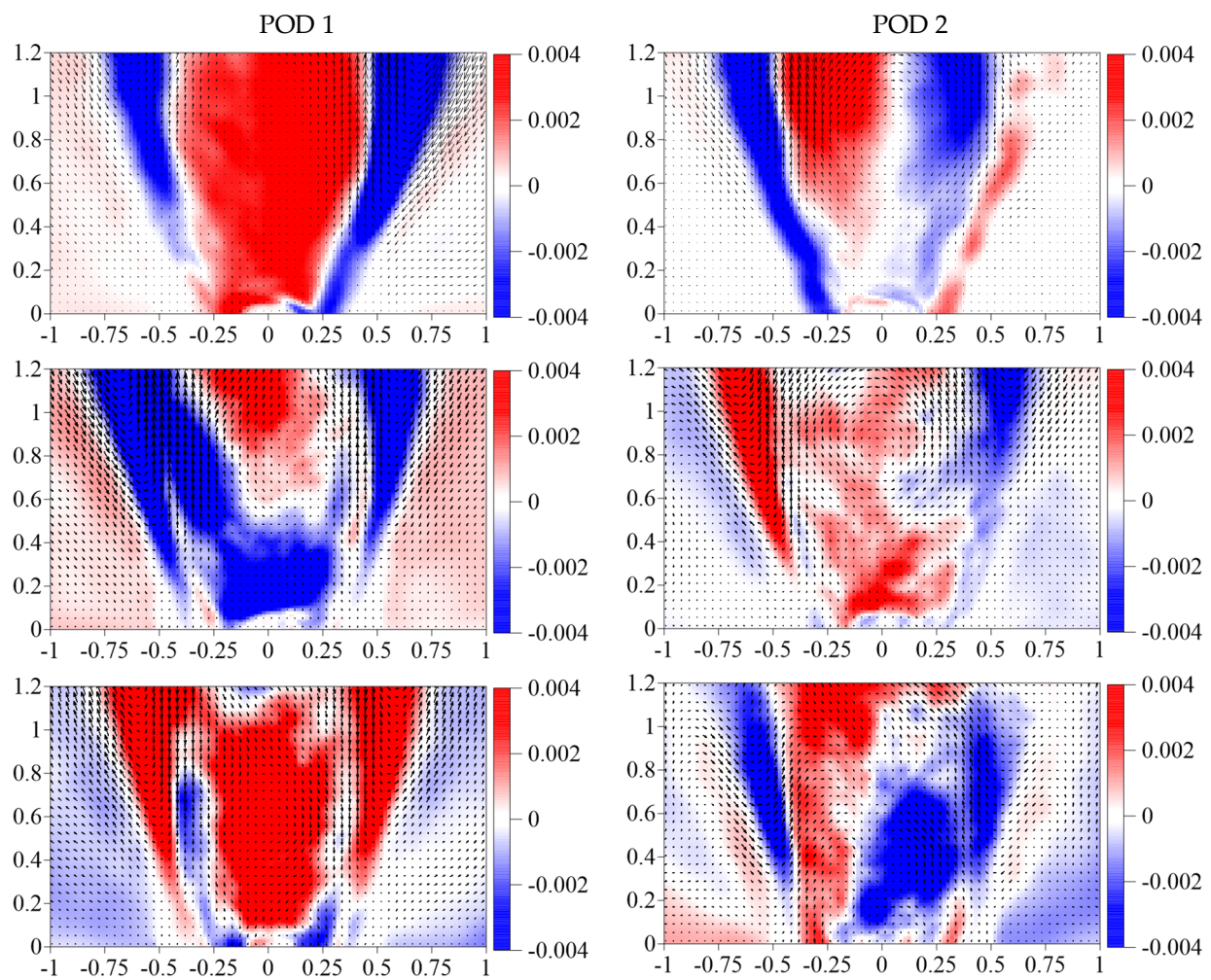


Figure 14. The first and the second POD modes with the conditionally sampled CO₂ concentration: the first line—1 atm, 293 K; the second line—2 atm, 500 K; the third line—3.4 atm, 500 K.

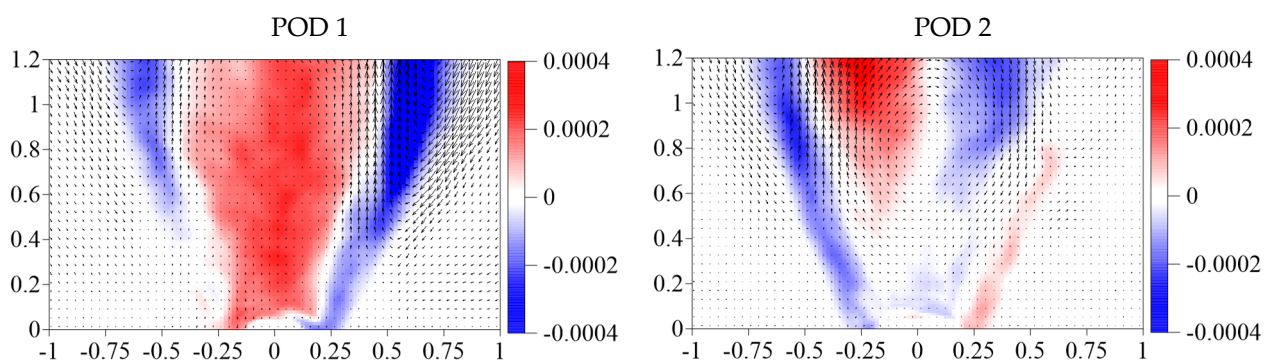


Figure 15. Cont.

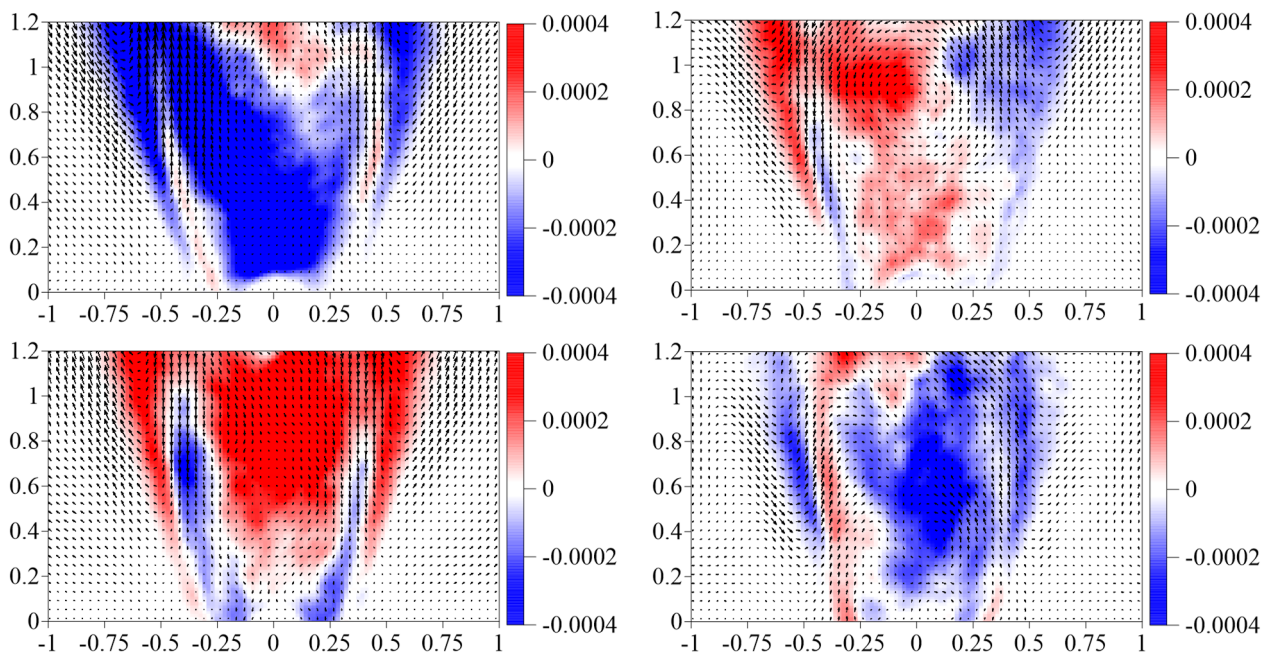


Figure 15. The first and the second POD modes with the conditionally sampled NO concentration: the first line—1 atm, 293 K; the second line—2 atm, 500 K; the third line—3.4 atm, 500 K.

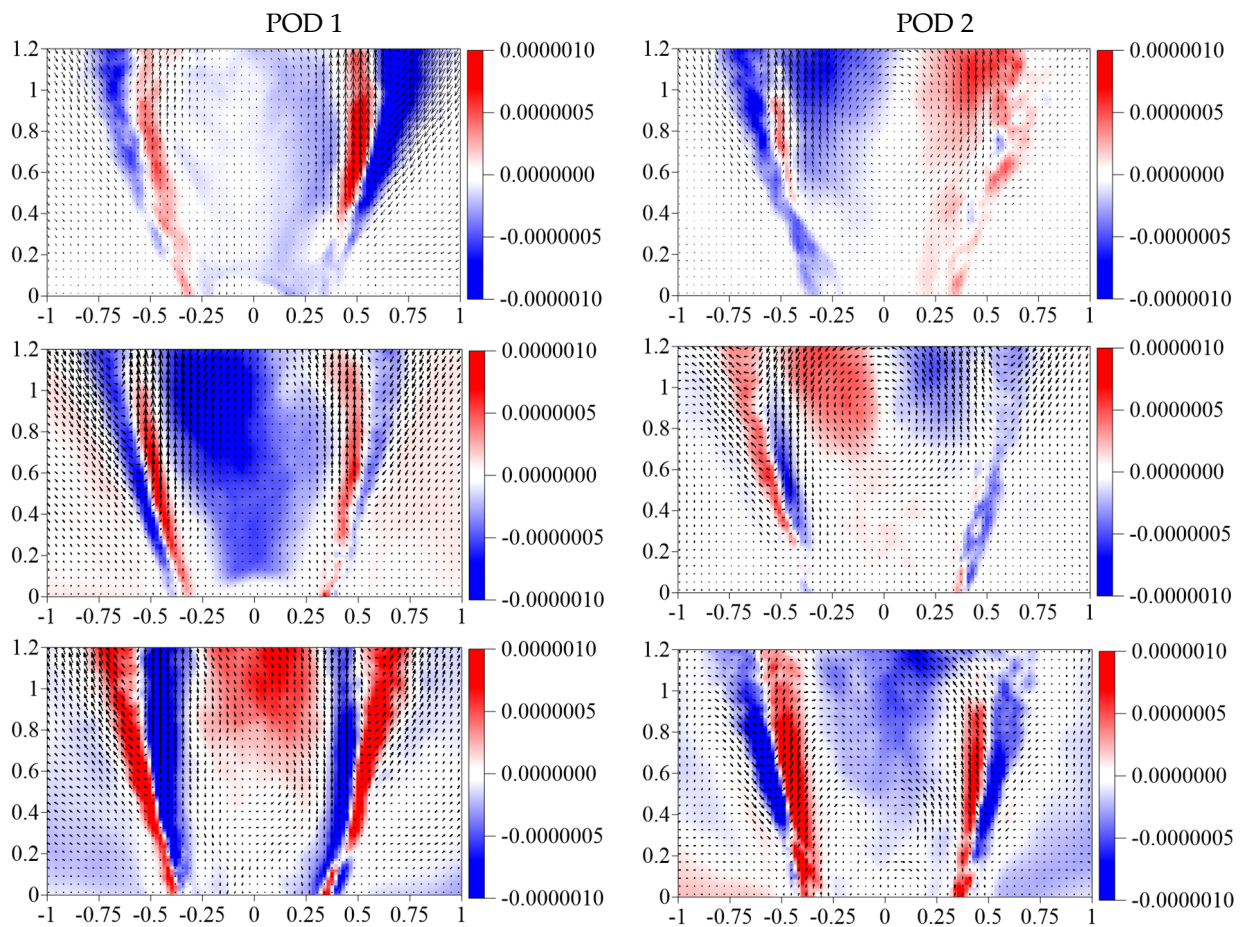


Figure 16. The first and the second POD modes with the conditionally sampled NO₂ concentration: the first line—1 atm, 293 K; the second line—2 atm, 500 K; the third line—3.4 atm, 500 K.

The longitudinal and transverse hydrodynamic modes are also related with sufficient fluctuations in the NO_2 concentration. However, the main difference is that the coherent fluctuations correspond mainly to the variations in the inner shear layer. It is also noteworthy that the amplitude of the coherent fluctuations for the elevated pressure and temperature increase sufficiently near the exit of the swirler's nozzle.

3.4. Coherent Flow Structures and Conditionally Sampled Data in Horizontal Cross-Sections

The Figures 17–22 demonstrate the results of the LES calculations of the flow field variations, temperature, and species concentrations and POD modes in horizontal cross-sections of the flow for the three cases at a distance of 1D from the burner exit. The spatial structure of the first four POD modes of the velocity variations is demonstrated in Figure 17; the normal to plane velocity components are shown by color. The spatial structure of the first three POD modes in case of atmospheric pressure demonstrates that POD does not separate the azimuthal hydrodynamic modes, with $m = 0$ and $m = \pm 1$. There is no corresponding symmetry in the distribution of these POD modes. The fourth POD mode seems to be dominated by the $m = \pm 2$ hydrodynamic mode.

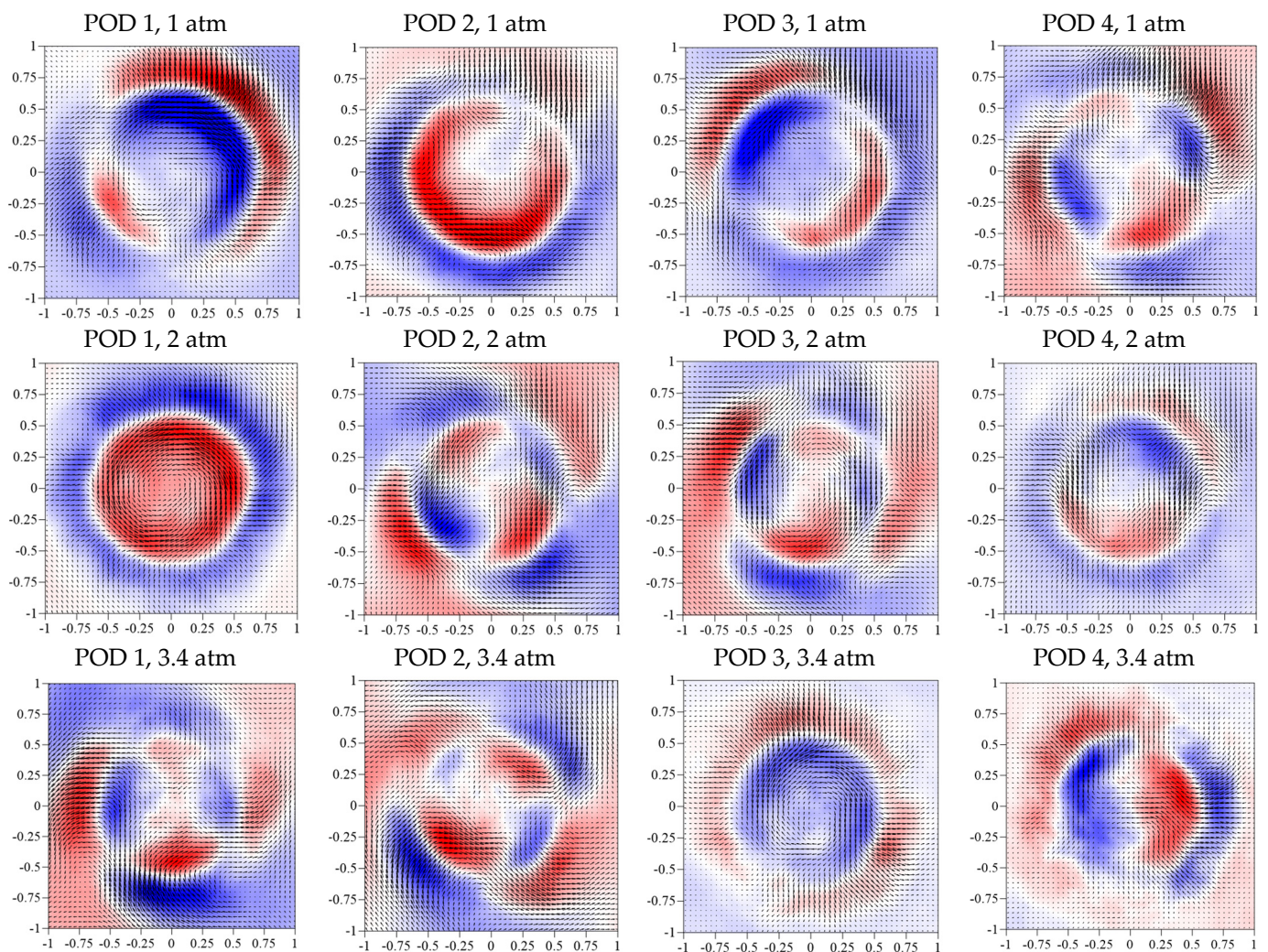


Figure 17. First four POD modes of the velocity variations (color scale demonstrates the out of plane velocity component variations) at a distance 1D from the nozzle exit.

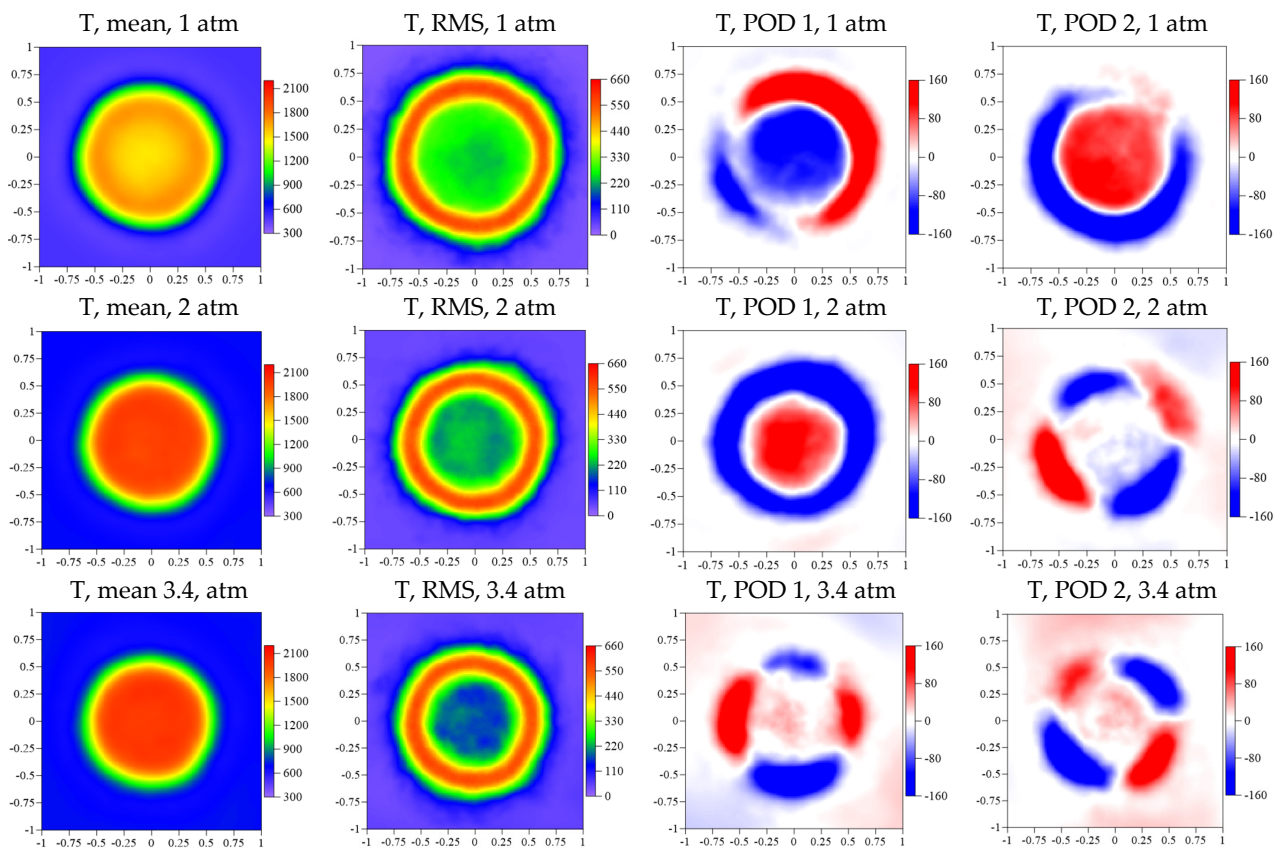


Figure 18. Mean and variations in the temperature field and the first and the second POD modes.

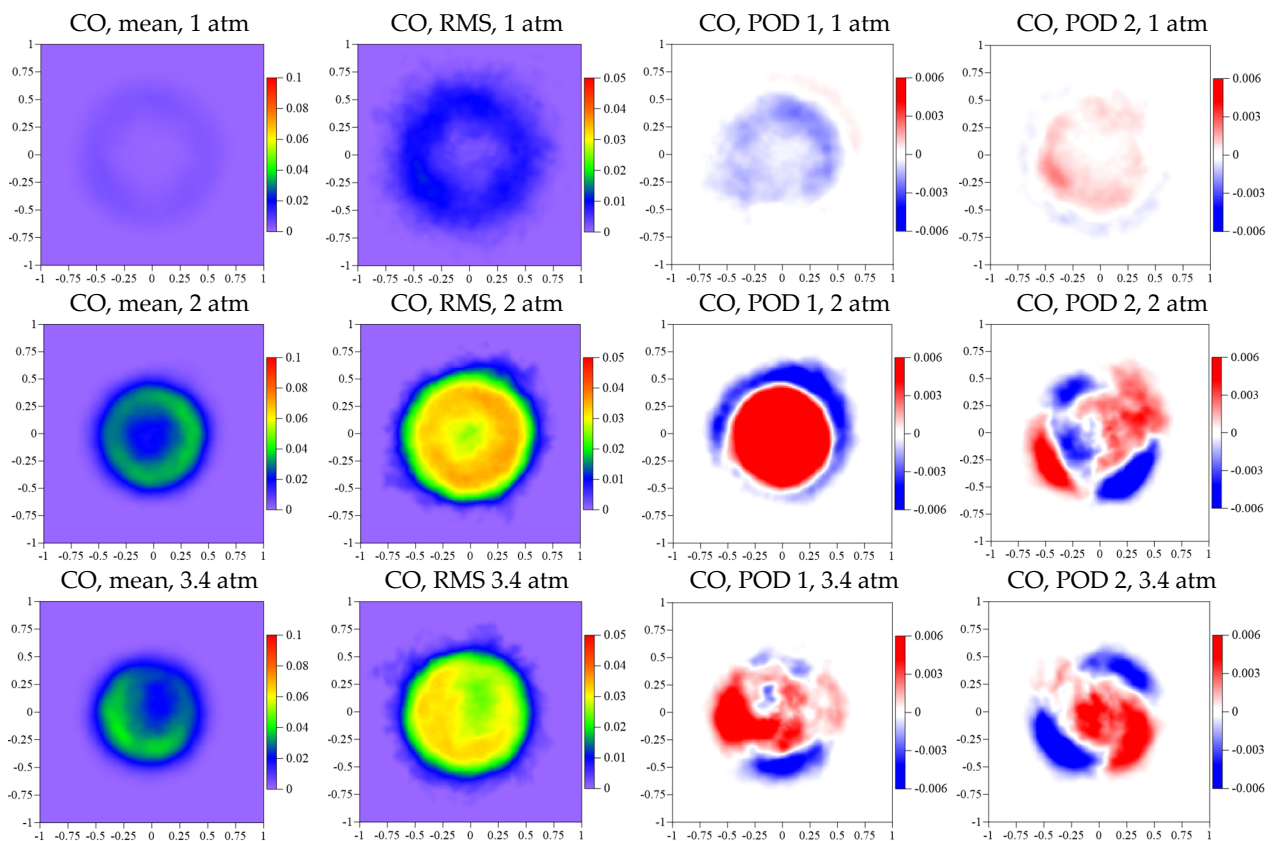


Figure 19. Mean and variation in the CO concentration field and the first and the second POD modes.

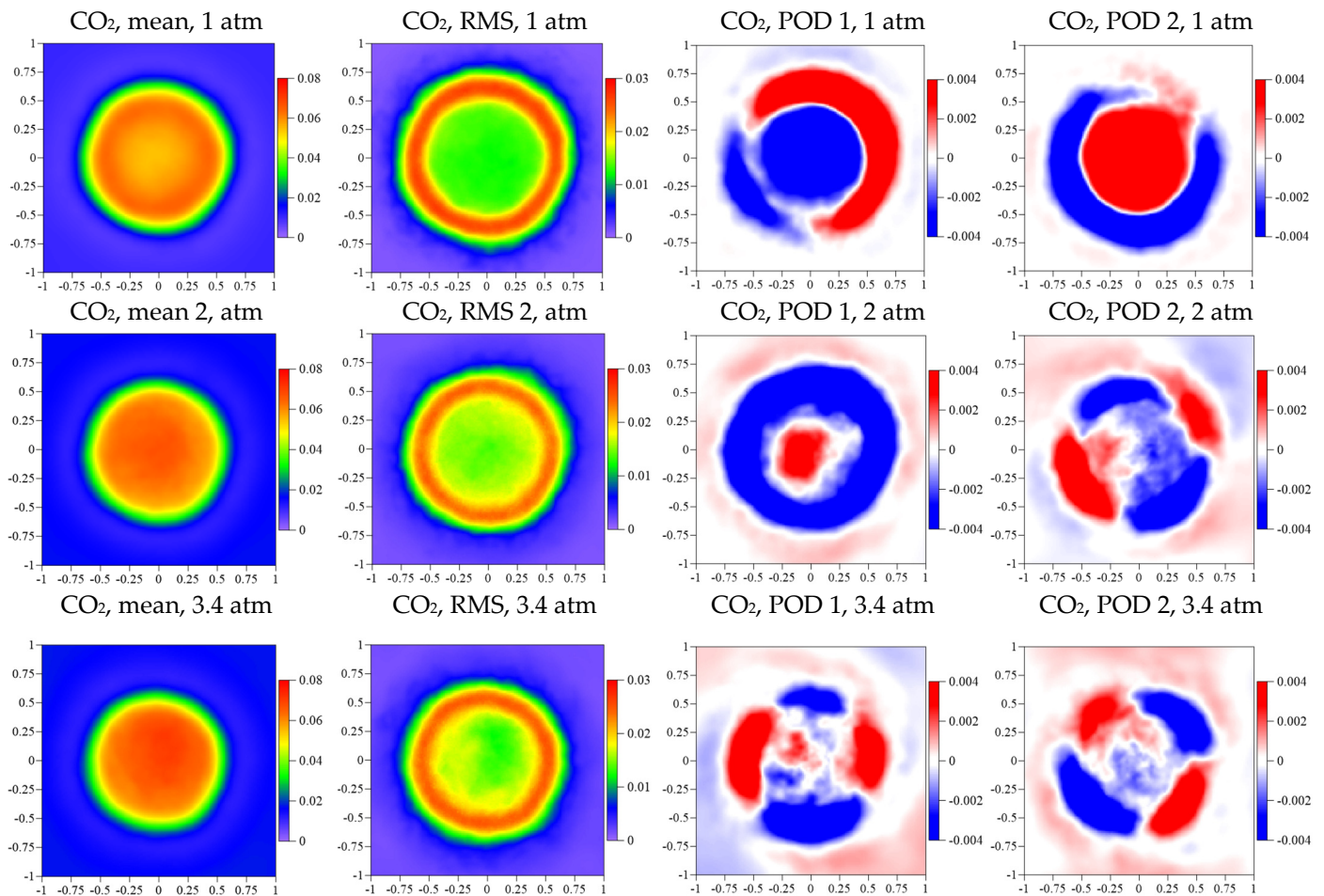


Figure 20. Mean and variation in the CO₂ concentration field and the first and second POD modes.

For the cases of elevated pressure and temperature there are traces of the $m = 0$ mode for POD 1 for 2 atm and POD 3 for 3.4 atm. The fourth POD mode seems to be related to $m = \pm 1$. The other two shown modes (POD 2 and POD 3 for 2 atm, and POD 1 and POD 2 for 3.4 atm) reveal hydrodynamic mode $m = \pm 2$, which was also reported for this swirler by Midgley et. Al. [20]. A trace of the coherent flow structures represented by this hydrodynamic mode we could observe in the distributions of the temperature fields (see Figure 18). In general, for all three cases we could observe the hot central zone with a radius of about $1D$ with the maxima of temperature variations in the ring-like region near the flame front. The temperature variations could locally reach up to 660 K. The contribution of only the first two POD modes could reach 160 K. As for the flow velocity variations, we could see that temperature variations are caused by a mix of the $m = 0$ and $m = \pm 1$ hydrodynamic modes in the case of atmospheric pressure. We could assign $m = 0$ as the first POD mode in the case of 2 atm pressure and the $m = \pm 2$ hydrodynamic mode as the second POD mode. For the 3.4 atm $m = \pm 2$ hydrodynamic mode, the impact is dominated in the temperature field variation's coherent structure.

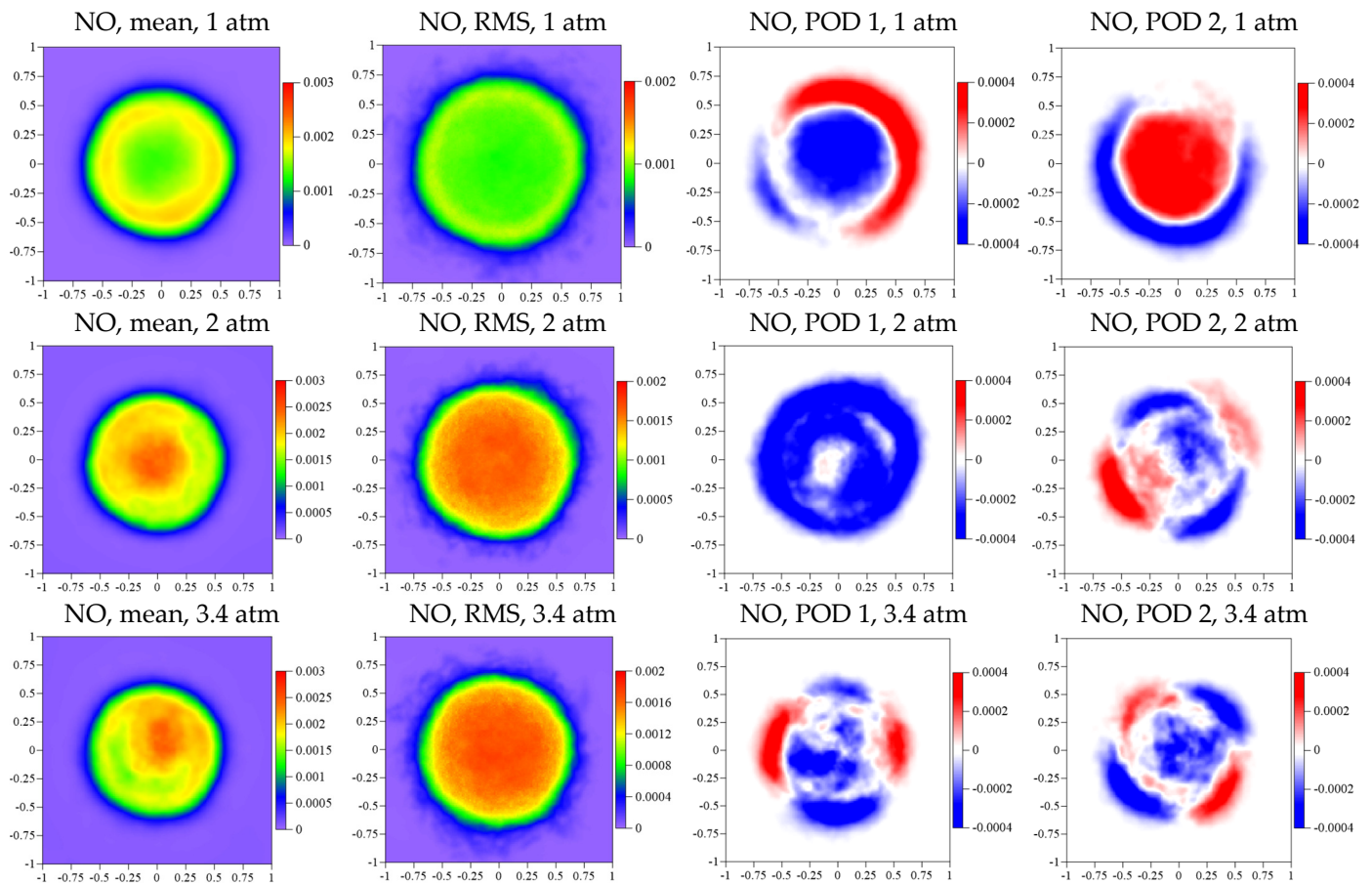


Figure 21. Mean and variation in the NO concentration field and the first and second POD modes.

If we look at the CO concentrations and its variations (see Figure 19), we could see that the absolute values of the CO concentrations and its variations are growing dramatically (about several times) with a pressure increase. We could observe the same influence of the corresponding hydrodynamic modes on the concentration variations fields, which are well correlated with temperature variations and corresponding POD modes. There is no significant difference in the values and spatial structure of the mean CO₂ concentrations and its variations for all three cases, but we can see a very good correlation of the first two POD modes with the temperature variations in the POD modes (see Figure 20).

Further analysis of NO concentration distributions and its variations (see Figure 21) shows that the spatial structure of the POD modes is well correlated with the coherent flow structures, which are demonstrated in the fields of temperature variations and CO/CO₂. The spatial distributions of NO₂ and its variations (see Figure 22) well correspond to the results for the axial cross-section of the flow (see Figure 10).

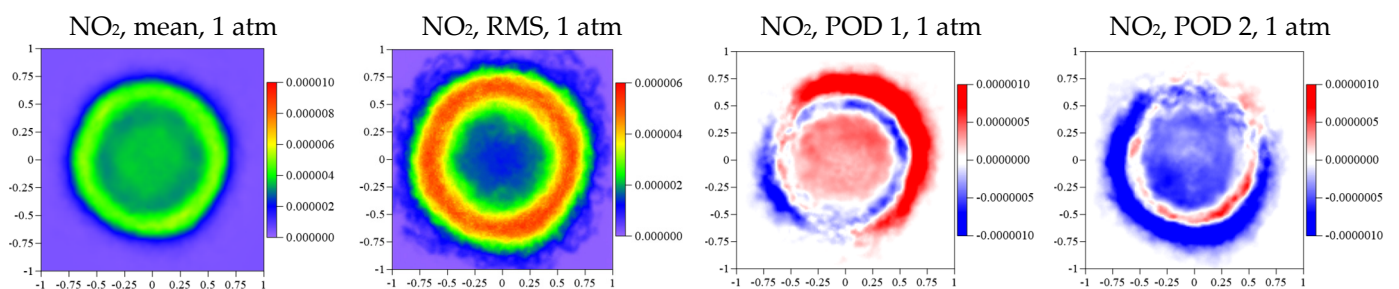


Figure 22. Cont.

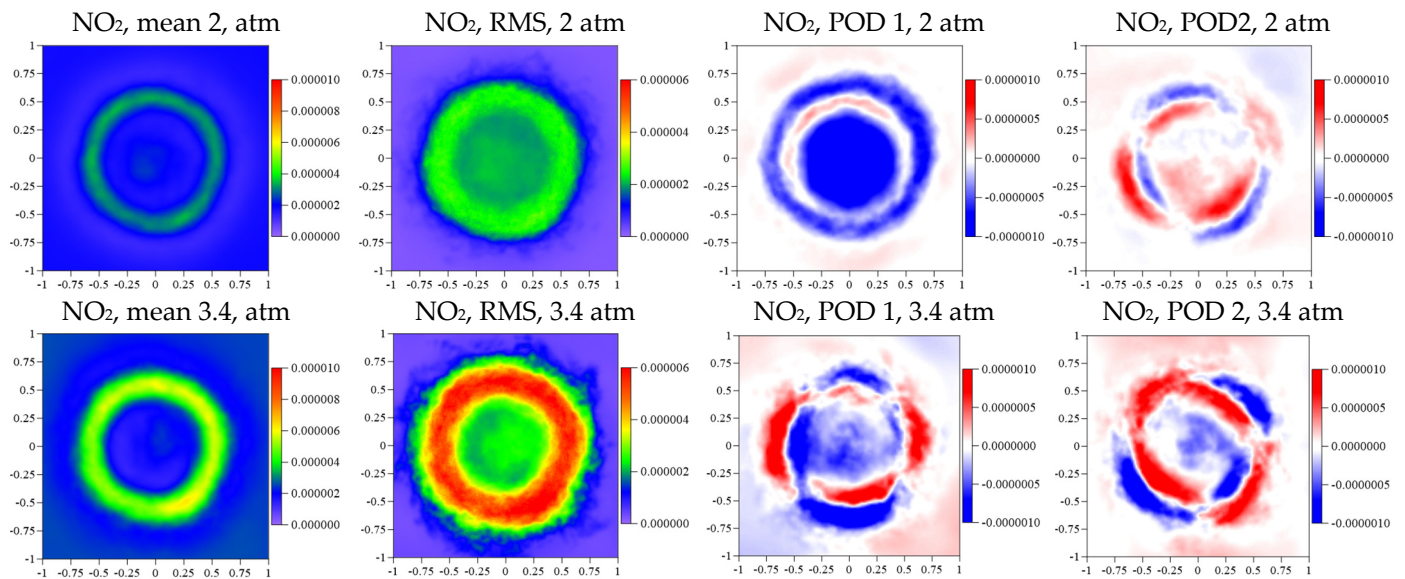


Figure 22. Mean and variation in the NO₂ concentration field and the first and second POD modes.

4. Conclusions

The numerical simulation of flow dynamics in a model gas-turbine combustor by large eddy simulation—in order to evaluate the effect of coherent flow structures on the local fluctuations of gas temperature and local concentrations of NO and CO—was carried out. The simulations were performed for the Reynolds number of 15,000 at a normal and elevated inlet temperature and pressure (up to 500 K and 3.4 atm). The methane–air flames were considered at normal conditions and at elevated pressure with the preheating of air up to 500 K. The global equivalence ratio was lean and close to the lean blowoff limit. The flame/flow interaction was studied by means of conditional sampling of LES data using a principal component analysis approach to reveal coherent large-scale structures in the turbulent pulsations of temperature and the products of combustion concentration fields, especially NO_x and CO.

For the elevated pressure and lower bulk velocity of the main air flow, the flame front shifts further inside the nozzle. The partial flash-back results in a worse mixing of the main fuel upstream of the flame front. This results in a reduced combustion efficiency and higher NO_x inside the swirler. Furthermore, it was found that the combustion of the central pilot flame becomes less stable for the elevated pressure and temperature, also resulting in a reduced combustion efficiency in the bottom part of the central recirculation zone (near the swirler) and causing a higher NO_x concentration downstream.

POD has been used to extract coherent flow structures and reveal induced local variations in temperature and concentration of nitrogen and carbon oxides. The temporal coefficients of the decomposition were used to evaluate the conditionally sampled spatial distributions of the temperature and species concentration. Longitudinal and transverse coherent flow structures were observed. It was shown that the contribution of the hydrodynamic modes to coherent temperature and oxide fluctuations could locally reach up to 200 K and up to 20% for NO, respectively. It shows that coherent flow structures in a lean swirl combustor can sufficiently contribute to NO_x emission. A hydrodynamic azimuthal mode, with $m = \pm 2$, was also detected, as previously reported by Midgley et al. [20].

Author Contributions: Conceptualization, D.M.M. and V.M.D.; methodology, L.M.C.; data processing, D.K.S., A.S.L. and A.A.D.; data acquisition, D.K.S. and R.V.T.; writing—original draft preparation, L.M.C.; writing—review and editing, V.M.D.; visualization, A.S.L.; supervision, V.M.D.; project administration, L.M.C.; funding acquisition, D.M.M. All authors have read and agreed to the published version of the manuscript.

Funding: Research was supported by the Ministry of Science and Higher Education of Russia, agreement No. 075-15-2020-806.

Institutional Review Board Statement: Not applicable.

Informed Consent Statement: Not applicable.

Data Availability Statement: The data that support the findings of this study are available from the corresponding author upon reasonable request.

Conflicts of Interest: The authors declare no conflict of interest.

Abbreviations

The following abbreviations are used in this manuscript:

LDI	Lean direct injection
GTMC	Gas-turbine model combustor
DLR	German Aerospace Center
LES	Large Eddy Simulation
URANS	Unsteady Reynolds-averaged Navier-Stokes
CFD	Computational fluid dynamics
PIV	Particle image velocimetry
PLIF	Planar laser-induced fluorescence
CCD	Charge-coupled device
Nd:YAG	Neodymium-doped yttrium aluminum garnet
sCMOS	Scientific complementary metal
oxide	Semiconductor
IRO	Intensified Reyleigh optics
UV	Ultraviolet
TTL	Transistor–transistor logic
WALE	Wall adapting local eddy-viscosity model
FGM	Flamelet generated manifold
DO	Discrete-ordinates
WSGGM	Weighted sum of grey gases model
SIMPLEC	Semi-implicit method for pressure linked equations-consistent
RANS	Reynolds-averaged Navier-Stokes
SST	Shear stress transport
HPC	High-performance computing
POD	Proper orthogonal decomposition
SVD	Singular value decomposition
CRZ	Central recirculation zone
RMS	Root mean square
D	Diameter of the swirler nozzle
(x, y, z)	Cartesian coordinate system components
U0	Bulk velocity
P	Pressure in combustion chamber
T	Temperature of the air

Appendix A. Effect of Grid Refinement and Soot Concentration

In order to study the grid convergence, a series of calculations of case 1 (1 atm and 293 K) was carried out for three types of grid with 2.9, 7.2, and 12 million nodes, respectively. Figures A1 and A2 represents the mean temperature and mean axial velocity profiles at a distance from the burner exit $y/D = 0.5$ for three meshes. It can be noted that the results obtained on a coarse grid (2.9 million of nodes) differ markedly from the results of medium (7.2 million of nodes) and detailed (12 million), both in terms of speed and temperature. A detailed grid with 12 million cells was chosen for further calculations.

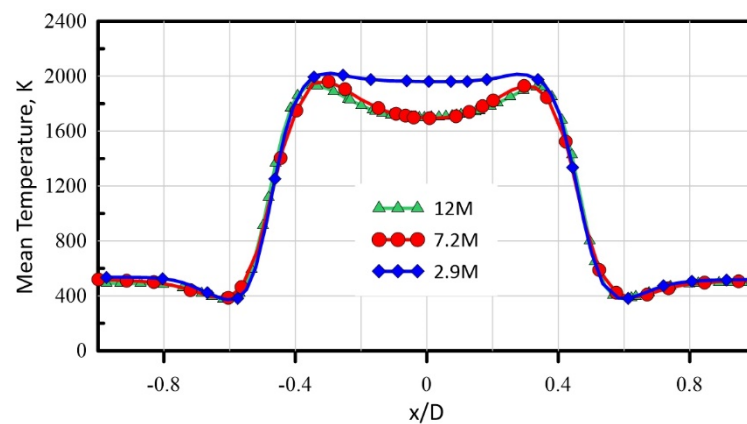


Figure A1. Mean temperature profiles depending on the mesh number of nodes, K.

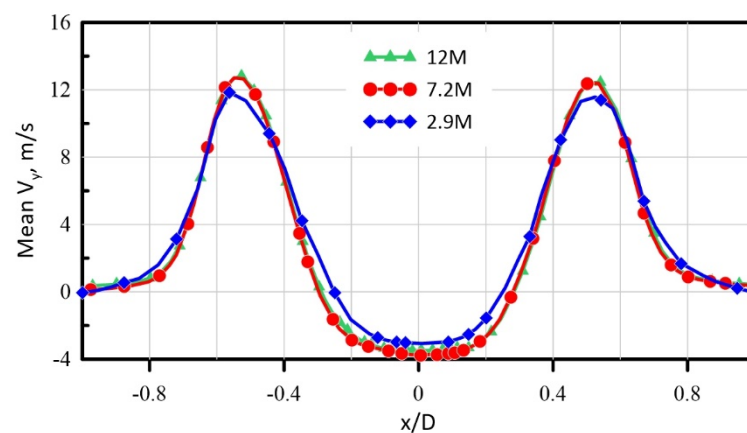


Figure A2. Mean axial velocity profiles for three types of meshes.

The soot concentration effect was estimated using the Moss–Brooks–Hall model for case 1 (1 atm and 293 K). This model shows a maximum volume concentration of soot of the order of 1–5 ppb, which is close to the values obtained in [36]. The distribution of the mean volume fraction of soot is shown in Figure A3. It can be noted that the maximum soot concentration is located near the exit from the nozzle. Using these data, the contribution of soot to the absorption coefficient of the medium has been evaluated according to S. S. Sazhin. “An Approximation for the Absorption Coefficient of Soot in a Radiating Gas”. Estimates have shown that soot makes an insignificant contribution to the absorption coefficient.

Absorption of soot can be estimated as:

$$a_s = b_1 \rho_g Y_{soot} [1 + b_T (T - 2000)] \quad (A1)$$

where $b_1 = 1232.4 \text{ m}^2/\text{kg}$, $b_T \approx 4.8 \cdot 10^{-4}$. Y_{soot} —soot mass fraction. The estimated value is less than 0.2% of the gas absorption coefficient. It shows that the effect of soot absorption and scattering is much less than other errors and the uncertainties of the model.

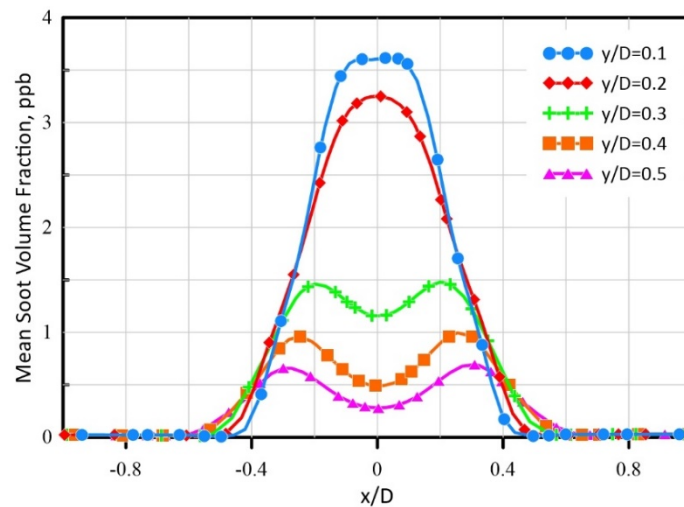


Figure A3. Mean soot volume fraction.

References

- Ren, X.; Brady, K.B.; Xue, X.; Sung, C.-J.; Mongia, H.C. Experimental investigation of lean-dome high-airflow airblast pilot mixers' operability, emissions, and dynamics. *Aerosp. Sci. Technol.* **2020**, *100*, 105829. [\[CrossRef\]](#)
- Mardani, A.; Rekabdarkolaei, B.A.; Rastaaghi, H.R.; Asadi, B. Experimental investigation on the effects of swirlers configurations and air inlet partitioning in a partially premixed double high swirl gas turbine model combustor. *J. Energy Resour. Technol.* **2021**, *143*, 012302. [\[CrossRef\]](#)
- El-Baz, A.M.; Roberts, W.L. Investigation of the effects of swirl and initial conditions on swirling non-premixed methane flames: Flow field, temperature, and species distributions. *Fuel* **2016**, *169*, 120–134. [\[CrossRef\]](#)
- Janus, B.; Dreizler, A.; Janicka, J. Experimental study on stabilization of lifted swirl flames in a model GT combustor. *Flow Turbul. Combust.* **2005**, *75*, 293–315. [\[CrossRef\]](#)
- Meier, W.; Weigand, P.; Duan, X.R.; Giezendanner-Thoben, R. Detailed characterization of the dynamics of thermoacoustic pulsations in a lean premixed swirl flame. *Combust. Flame* **2007**, *150*, 2–26. [\[CrossRef\]](#)
- Boxx, I.; Arndt, C.M.; Carter, C.D.; Meier, W. High-speed laser diagnostics for the study of flame dynamics in a lean premixed gas turbine model combustor. *Exp. Fluids* **2012**, *52*, 555–567. [\[CrossRef\]](#)
- Albrecht, P.; Bade, S.; Lacarelle, A.; Paschereit, C.O.; Gutmark, E. Instability control by premixed pilot flames. *J. Eng. Gas Turbines Power-Trans. ASME* **2010**, *132*, 041501. [\[CrossRef\]](#)
- Liu, C.; Liu, F.; Yang, J.; Mu, Y.; Hu, C.; Xu, G.; Su, S. Improvement on ignition and lean blowout performances of a piloted lean-burn combustor. *Proc. Inst. Mech. Eng. Part A J. Power Energy* **2016**, *230*, 196–205. [\[CrossRef\]](#)
- Boxx, I.; Slabaugh, C.; Kutne, P.; Lucht, R.; Meier, W. 3 kHz PIV/OH-PLIF measurements in a gas turbine combustor at elevated pressure. *Proc. Combust. Inst.* **2015**, *35*, 3793–3802. [\[CrossRef\]](#)
- Stopper, U.; Aigner, M.; Meier, W.; Sadanandan, R.; Stöhr, M.; Kim, I.S. Flow Field and Combustion Characterization of Premixed Gas Turbine Flames by Planar Laser Techniques. *J. Eng. Gas Turbines Power* **2009**, *131*, 021504. [\[CrossRef\]](#)
- Sung, H.-G. Combustion dynamics in a model lean-premixed gas turbine with a swirl stabilized injector. *J. Mech. Sci. Technol.* **2007**, *21*, 495–504. [\[CrossRef\]](#)
- Zettervall, N.; Worth, N.A.; Mazur, M.; Dawson, J.R.; Fureby, C. Large eddy simulation of CH₄-air and C₂H₄-air combustion in a model annular gas turbine combustor. *Proc. Combust. Inst.* **2017**, *37*, 5223–5231. [\[CrossRef\]](#)
- Semlitsch, B.; Hynes, T.; Langella, I.; Swaminathan, N.; Dowling, A.P. Entropy and vorticity wave generation in realistic gas turbine combustors. *J. Propuls. Power* **2019**, *35*, 839–849. [\[CrossRef\]](#)
- Agostinelli, P.W.; Laera, D.; Boxx, I.; Gicquel, L.; Poinot, T. Impact of wall heat transfer in Large Eddy Simulation of flame dynamics in a swirled combustion chamber. *Combust. Flame* **2021**, *234*, 111728. [\[CrossRef\]](#)
- Yin, Z.; Nau, P.; Meier, W. Responses of combustor surface temperature to flame shape transitions in a turbulent bi-stable swirl flame. *Exp. Therm. Fluid Sci.* **2017**, *82*, 50–57. [\[CrossRef\]](#)
- Roux, S.; Lartigue, G.; Poinot, T.; Meier, U.; Bérat, C. Studies of mean and unsteady flow in a swirled combustor using experiments, acoustic analysis, and large eddy simulations. *Combust. Flame* **2005**, *141*, 40–54. [\[CrossRef\]](#)
- Moureau, V.; Domingo, P.; Vervisch, L. From large-eddy simulation to direct numerical simulation of a lean premixed swirl flame: Filtered laminar flame-pdf modeling. *Combust. Flame* **2011**, *158*, 1340–1357. [\[CrossRef\]](#)
- Huang, Y.; Sung, H.-G.; Hsieh, S.-Y.; Yang, V. Large-eddy simulation of combustion dynamics of lean-premixed swirl-stabilized combustor. *J. Propuls. Power* **2003**, *19*, 782–794. [\[CrossRef\]](#)
- Gicquel, L.Y.M.; Staffelbach, G.; Poinot, T. Large eddy simulations of gaseous flames in gas turbine combustion chambers. *Prog. Energy Combust.* **2012**, *38*, 782–817. [\[CrossRef\]](#)

20. Schiavo, E.L.; Laera, D.; Riber, E.; Gicquel, L.; Poinot, T. Effects of liquid fuel/wall interaction on thermoacoustic instabilities in swirling spray flames. *Combust. Flame* **2020**, *219*, 86–101. [[CrossRef](#)]
21. Sharaborin, D.K.; Savitskii, A.G.; Bakharev, G.Y.; Lobasov, A.S.; Chikishev, L.M.; Dulin, V.M. PIV/PLIF investigation of unsteady turbulent flow and mixing behind a model gas turbine combustor. *Exp. Fluids* **2021**, *62*, 96. [[CrossRef](#)]
22. Midgley, K.; Spencer, A.; McGuirk, J.J. Unsteady Flow Structures in Radial Swirler Fed Fuel Injectors. *ASME J. Eng. Gas Turbines Power* **2005**, *127*, 755–764. [[CrossRef](#)]
23. Dunham, D.; Spencer, A.; McGuirk, J.; Dianat, M. Comparison of unsteady Reynolds averaged Navier Stokes and Large Eddy Simulation CFD Methodologies for air swirl fuel injectors. *ASME J. Eng. Gas Turbines Power* **2009**, *131*, 011502-1–011502-8. [[CrossRef](#)]
24. Smith, G.P. Gri-Mech 3.0. 1999. Available online: https://www.me.berkeley.edu/gri_mech/ (accessed on 9 September 2020).
25. Chui, E.H.; Raithby, G.D. Computation of Radiant Heat Transfer on a Non-Orthogonal Mesh Using the Finite-Volume Method. *Numer. Heat Transf. Part B* **1993**, *23*, 269–288. [[CrossRef](#)]
26. Murthy, J.Y.; Mathur, S.R. Finite Volume Method for Radiative Heat Transfer Using Unstructured Meshes. *J. Thermophys. Heat Transf.* **1998**, *12*, 313–321. [[CrossRef](#)]
27. Smith, T.F.; Shen, Z.F.; Friedman, J.N. Evaluation of Coefficients for the Weighted Sum of Gray Gases Model. *J. Heat Transf.* **1982**, *104*, 602–608. [[CrossRef](#)]
28. Vandoormaal, J.P.; Raithby, G.D. Enhancements of the SIMPLE Method for Predicting Incompressible Fluid Flows. *Numer. Heat Transf.* **1984**, *7*, 147–163.
29. Scarano, F. Iterative image deformation methods in PIV. *Meas. Sci. Technol.* **2001**, *13*, R1–R19. [[CrossRef](#)]
30. Soloff, S.M.; Adrian, R.J.; Liu, Z.-C. Distortion compensation for generalized stereoscopic particle image velocimetry. *Meas. Sci. Technol.* **1997**, *8*, 1441–1454. [[CrossRef](#)]
31. Sirovich, L.; Kirby, M. Turbulence and dynamics of coherent structures. Part I: Coherent structures. *Q. Appl. Math.* **1987**, *45*, 561–571. [[CrossRef](#)]
32. Kerschen, G.; Golinval, J.-C.; Vakakis, A.F.; Bergman, L.A. The method of proper orthogonal decomposition for dynamical characterization and order reduction of mechanical systems: An overview. *Nonlinear Dyn.* **2005**, *41*, 147–169. [[CrossRef](#)]
33. Duwig, C.; Fuchs, L. Large eddy simulation of vortex breakdown/flame interaction. *Phys. Fluids* **2007**, *19*, 075103. [[CrossRef](#)]
34. Lobasov, A.S.; Alekseenko, S.V.; Markovich, D.M.; Dulin, V.M. Mass and momentum transport in the near field of swirling turbulent jets. Effect of swirl rate. *Int. J. Heat Fluid Flow* **2020**, *83*, 108539. [[CrossRef](#)]
35. Dulin, V.; Chikishev, L.; Sharaborin, D.; Lobasov, A.; Tolstoguzov, R.; Liu, Z.; Shi, X.; Li, Y.; Markovich, D. On the Flow Structure and Dynamics of Methane and Syngas Lean Flames in a Model Gas-Turbine Combustor. *Energies* **2021**, *14*, 8267. [[CrossRef](#)]
36. Wang, L.-Y.; Chatterjee, S.; An, Q.; Steinberg, A.M.; Gülder, Ö.L. Soot formation and flame structure in swirl-stabilized turbulent non-premixed methane combustion. *Combust. Flame* **2019**, *209*, 303–312. [[CrossRef](#)]